AD-A183 143 A MID-LATITUDE SCINTILLATION MODEL(U) NORTHWEST 1/1
RESEARCH ASSOCIATES INC BELLEVUE WA R E ROBINS ET AL
31 OCT 86 NWRA-86-R004 DNA-TR-86-381 DNA001-85-C-0017
UNCLASSIFIED F/G 4/1 NL

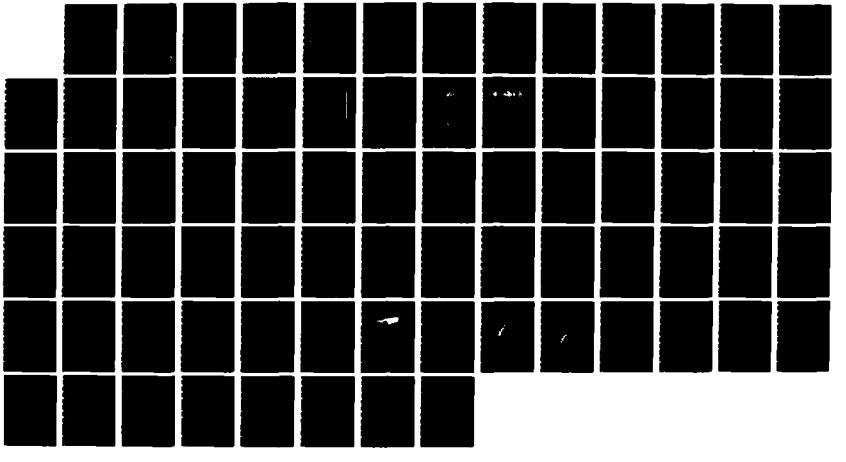

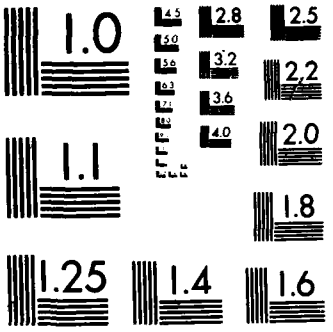

DNA-TR-86-381

A MID-LATITUDE SCINTILLATION MODEL

R. E. Robins
J. A. Secan
E. J. Fremouw
Northwest Research Associates, Inc.
P. O. Box 3027
Bellevue, WA 98009-3027

31 October 1986

Technical Report

CONTRACT No. DNA 001-85-C-0017

Approved for public release;
distribution is unlimited.

THIS WORK WAS SPONSORED BY THE DEFENSE NUCLEAR AGENCY
UNDER RDT&E RMC CODE B3220854662 RI RO 00122 25904D.

Prepared for
Director
DEFENSE NUCLEAR AGENCY
Washington, DC 20305-1000

Destroy this report when it is no longer needed. Do not return to sender.

PLEASE NOTIFY THE DEFENSE NUCLEAR AGENCY ATTN: TITL, WASHINGTON, DC 20305 1000, IF YOUR ADDRESS IS INCORRECT, IF YOU WISH IT DELETED FROM THE DISTRIBUTION LIST, OR IF THE ADDRESSEE IS NO LONGER EMPLOYED BY YOUR ORGANIZATION.

DISTRIBUTION LIST UPDATE

This mailer is provided to enable DNA to maintain current distribution lists for reports. We would appreciate your providing the requested information.

☐ Add the individual listed to your distribution list.

☐ Delete the cited organization/individual.

☐ Change of address.

NAME: _____

ORGANIZATION: _____

OLD ADDRESS	CURRENT ADDRESS
_____	_____
_____	_____
_____	_____

TELEPHONE NUMBER: ( ) _____

SUBJECT AREA(s) OF INTEREST:

_____	_____
_____	_____
_____	_____

DNA OR OTHER GOVERNMENT CONTRACT NUMBER: _____

CERTIFICATION OF NEED-TO-KNOW BY GOVERNMENT SPONSOR (if other than DNA):

SPONSORING ORGANIZATION: _____

CONTRACTING OFFICER OR REPRESENTATIVE: _____

SIGNATURE: _____

Director
Defense Nuclear Agency
ATTN: [redacted] TITL
Washington, DC 20305-1000

Director
Defense Nuclear Agency
ATTN: [redacted] TITL
Washington, DC 20305-1000

REPORT DOCUMENTATION PAGE

1a. REPORT SECURITY CLASSIFICATION UNCLASSIFIED	1b. RESTRICTIVE MARKINGS
2a. SECURITY CLASSIFICATION AUTHORITY N/A since Unclassified	3. DISTRIBUTION/AVAILABILITY OF REPORT Approved for public release; distribution is unlimited.
2b. DECLASSIFICATION/DOWNGRADING SCHEDULE N/A since Unclassified	
4. PERFORMING ORGANIZATION REPORT NUMBER(S) NWRA-86-R004	5. MONITORING ORGANIZATION REPORT NUMBER(S) DNA-TR-86-381
6a. NAME OF PERFORMING ORGANIZATION Northwest Research Associates, Inc. 6b. OFFICE SYMBOL (If applicable) NWRA	7a. NAME OF MONITORING ORGANIZATION Director Defense Nuclear Agency
6c. ADDRESS (City, State, and ZIP Code) P.O. Box 3027 Bellevue, WA 98009-3027	7b. ADDRESS (City, State, and ZIP Code) Washington, DC 20305-1000
8a. NAME OF FUNDING/SPONSORING ORGANIZATION 8b. OFFICE SYMBOL (If applicable) RAAE/Wittwer	9. PROCUREMENT INSTRUMENT IDENTIFICATION NUMBER DNA 001-85-C-0017
8c. ADDRESS (City, State, and ZIP Code)	10. SOURCE OF FUNDING NUMBERS PROGRAM ELEMENT NO. 62715H; PROJECT NO. RI; TASK NO. RO; WORK UNIT ACCESSION NO. DH008620
11. TITLE (Include Security Classification) A MID-LATITUDE SCINTILLATION MODEL	
12. PERSONAL AUTHOR(S) Robins, Robert E.; Secan, James A.; Fremouw, E.J.	
13a. TYPE OF REPORT Technical 13b. TIME COVERED FROM 851101 TO 861031	14. DATE OF REPORT (Year, Month, Day) 861031 15. PAGE COUNT 78
16. SUPPLEMENTARY NOTATION This work was sponsored by the Defense Nuclear Agency under RDT&E RMC Code B3220854662 RI RO 00122 25904D.	

17. COSATI CODES			18. SUBJECT TERMS (Continue on reverse if necessary and identify by block number)
FIELD	GROUP	SUB-GROUP	Structured High-altitude Plasmas; Transionospheric Radio and Radar Channels; Radiowave Scintillation; Mid-latitude Scintillation
13	2		
2	8		

19. ABSTRACT (Continue on reverse if necessary and identify by block number)

Radiowave scintillation in the presence of ionospheric disturbances has the potential to disrupt numerous transionospheric radio and radar systems. This report describes development of a model characterizing the plasma-density irregularities that produce scintillation in the naturally disturbed mid-latitude F layer. The model will be incorporated into Program WBMOD, which includes subroutines for computing both link geometry and scintillation indices, the latter by means of phase-screen diffraction theory. Earlier versions of WBMOD, which are operational at USAF Global Weather Central and at several other user locations, were based on extensive analysis of scintillation data collected in the auroral and equatorial zones in DNA's Wideband Satellite Mission. The model described herein is based on similarly extensive analysis of Wideband data from one mid-latitude station and of data collected from DNA's HiLat satellite at another mid-latitude station. The model describes irregularities

20. DISTRIBUTION/AVAILABILITY OF ABSTRACT ☐ UNCLASSIFIED/UNLIMITED ☒ SAME AS RPT. ☐ DTIC USERS	21. ABSTRACT SECURITY CLASSIFICATION UNCLASSIFIED
22a. NAME OF RESPONSIBLE INDIVIDUAL Sandra E. Young	22b. TELEPHONE (Include Area Code) (202) 325-7042 22c. OFFICE SYMBOL DNA/CSTI

DD FORM 1473, 84 MAR 83 APR edition may be used until exhausted. All other editions are obsolete.

19. ABSTRACT (Continued)

at an effective height of 350 km that are isotropic across the geomagnetic field and elongated by a factor of 10 along the field and whose one-dimensional spatial power spectrum obeys a single-regime power law with a (negative) spectral index of 1.5. The height-integrated spectral strength of the irregularities is modeled as a function of magnetic apex local time, solar epoch (sunspot number), and the F-layer magnetic apex latitude of the point. The report highlights a disagreement by a factor of approximately three between irregularity strength inferred from the two satellites in a region of overlap between the two mid-latitude stations. Whether this difference results from processing artifacts or geophysical processes is still open to investigation.

CONVERSION TABLE

Conversion factors for U.S. customary to metric (SI) units of measurement.

To Convert From	To	Multiply By
angstrom	meters (m)	1.000 000 X E -10
atmosphere (normal)	kilo pascal (kPa)	1.013 25 X E +2
bar	kilo pascal (kPa)	1.000 000 X E +2
barn	meter^2 (m^2)	1.000 000 X E -28
British thermal unit (thermochemical)	joule (J)	1.054 350 X E +3
calorie (thermochemical)	joule (J)	4.184 000
cal (thermochemical)/cm^2	mega joule/m^2 (MJ/m^2)	4.184 000 X E -2
degree (angle)	radian (rad)	1.745 329 X E -2
degree Fahrenheit	degree kelvin (K)	$t_K = (t°f + 459.67)/1.8$
electron volt	joule (J)	1.602 19 X E -19
erg	joule (J)	1.000 000 X E -7
erg/second	watt (W)	1.000 000 X E -7
foot	meter (m)	3.048 000 X E -1
foot-pound-force	joule (J)	1.355 818
gallon (U.S. liquid)	meter^3 (m^3)	3.785 412 X E -3
inch	meter (m)	2.540 000 X E -2
jerk	joule (J)	1.000 000 X E +9
kip (1000 lbf)	newton (N)	4.448 222 X E +3
kip/inch^2 (ksi)	kilo pascal (kPa)	6.894 757 X E +3
ktap	newton-second/m^2 ($N-s/m^2$)	1.000 000 X E +2
micron	meter (m)	1 000 000 X E -6
mil	meter (m)	2.540 000 X E -5
mile (international)	meter (m)	1.609 344 X E +3
ounce	kilogram (kg)	2.834 952 X E -2
pound-force (lbs avoirdupois)	newton (N)	4.448 222
pound-force inch	newton-meter (N·m)	1.129 848 X E -1
pound-force/inch	newton/meter (N/m)	1.751 268 X E +2
pound-force/foot^2	kilo pascal (kPa)	4.788 026 X E -2
pound-force/inch^2 (psi)	kilo pascal (kPa)	6.894 757
pound-mass (lbm avoirdupois)	kilogram (kg)	4.535 924 X E -1
pound-mass-foot^2 (moment of inertia)	kilogram-meter^2 ($kg·m^2$)	4.214 011 X E -2
pound-mass/foot^3	kilogram/meter^3 (kg/m^3)	1.601 846 X E +1
roentgen	coulomb/kilogram (C/kg)	2.579 760 X E -4
shake	second (s)	1 000 000 X E -8
slug	kilogram (kg)	1.459 390 X E +1
torr (mm Hg, 0° C)	kilo pascal (kPa)	1.333 22 X E -1

TABLE OF CONTENTS

LIST OF ILLUSTRATIONS

LIST OF TABLES

SECTION 1

INTRODUCTION

A recent report (Fremouw and Robins, 1985) described a scintillation model for equatorial regions. This model was incorporated into the computer program WBMOD to complement a previously developed scintillation model for auroral regions (Fremouw and Lansinger, 1981; Secan and Fremouw, 1983a). Both models were based on extensive analysis of data from DNA's Wideband Satellite (Rino *et al*, 1977; Fremouw *et al*, 1978).

In this report we describe the determination of a mid-latitude scintillation model. The model is based on Wideband data taken at Stanford, CA, and on a subset of the data taken at Bellevue, WA, from the DNA Hilat satellite (Fremouw *et al*, 1985). The Wideband mid-latitude data set is significantly smaller than the Wideband equatorial and auroral data sets, since mid-latitude data were obtained only for the first four months (May 1976 to Sept. 1976) of the Wideband experiment. The Stanford receiver subsequently was moved to Kwajalein to obtain equatorial data for the duration of the experiment (until Sept. 1979).

In spite of the limited data base available from Stanford, we were able to use it to obtain useful parameterizations of the irregularity-layer height, latitudinal dependence, and average strength. The mid-latitude data taken with the transportable HiLat receiver, "Rover," while located at Bellevue, WA, during the period April 1984 through February 1986 were used to obtain the diurnal variation and to determine the solar-cycle dependence of the scintillation level at mid-latitudes. Representations of mid-latitude convective drift and along-field axial ratio were determined from published results.

In Section 2 we describe the Stanford and Bellevue data bases and briefly review the modeling approach, which was described in detail in the previous report (Fremouw and Robins, 1985). In Section 3 we explain our choices for mid-latitude plasma-drift velocity, shape factors, and height of the equivalent phase screen. In Section 4 we describe our determination of the model for the height-integrated spectral strength of irregularities. We depart from the approach used for equatorial and auroral modeling in two ways. First, instead of expressing spectral strength in terms of the familiar $C_s L$, we use the quantity $C_k L$, defined by

$$C_k L = \left(\frac{1000}{2} \text{ meters}\right)^{1+p} C_s L \qquad (1)$$

where p is the phase power-law spectral index. The reason for this change is discussed in Appendix A. Second, as we discuss further in Section 4, the statistics of the data have led us to model log $C_k L$ rather than $C_k L$. In Section 5 we conclude by showing some model vs data comparisons to demonstrate the utility of the model, and by summarizing our work.

SECTION 2

METHOD

2.1 STANFORD DATA.

The Wideband receiver at Stanford was located at 37°26'N, 122 10'W (apex latitude and longitude* of 43.14°N and 299.93°E, respectively). From May 28 to September 10, 1976, data from 87 passes were received; 63 of these passes (2536 points) were at night (2300 to 0050) and 24 passes (941 points) were during the day (0945 to 1125). Figures 1(a) and 1(b) show scatter plots of F layer (350 km) penetration point locations for all passes in the Stanford data base except for three. (Two night and one day pass were deleted for reasons explained below.) In both plots, the receiver location is shown as a small circle. Figure 1(a) shows the penetration point distribution on a grid of geographic latitude and longitude and Figure 1(b) shows it on a grid of apex latitude and longitude. The data fall into distinct corridors, which we have labeled N1, N2, N3, N4, N5, and N6 for nighttime passes and D1, D2, D3, D4, and D5 for daytime passes. The direction of the nighttime passes was from north to south and for the daytime passes was from south to north.

Two passes were deleted because of severe tracking errors. Because the number of daytime passes was relatively small, two daytime passes with less severe tracking errors were retained. (Errant penetration points from these passes are evident between corridors D1 and D2.) A third pass was dropped because of unusually large σ_ϕ (rms phase fluctuation) values. Figure 2 shows a scatter plot of nighttime σ_ϕ *vs* λ_a (apex latitude) points, with points from the third deleted pass shown as small circles. The K_p value at the time of the anomalous pass was 4+ (4.33) and, 1.5 hours after the pass, it was 7- (6.67), which was the highest K_p value that occurred during the Stanford campaign. This coincidence of high K_p and high σ_ϕ is quite suggestive that magnetic storm activity was an influence on the unusually strong phase scintillation. In any case, the pass was deleted from the data set to prevent it from biasing the various scintillation statistics.

The result of the above pass deletions and the removal of two additional bad points was to leave the Stanford data base with 61 nighttime passes containing 2447

---

*The use of apex coordinates in WBMOD is described by Secan and Fremouw, 1983b.

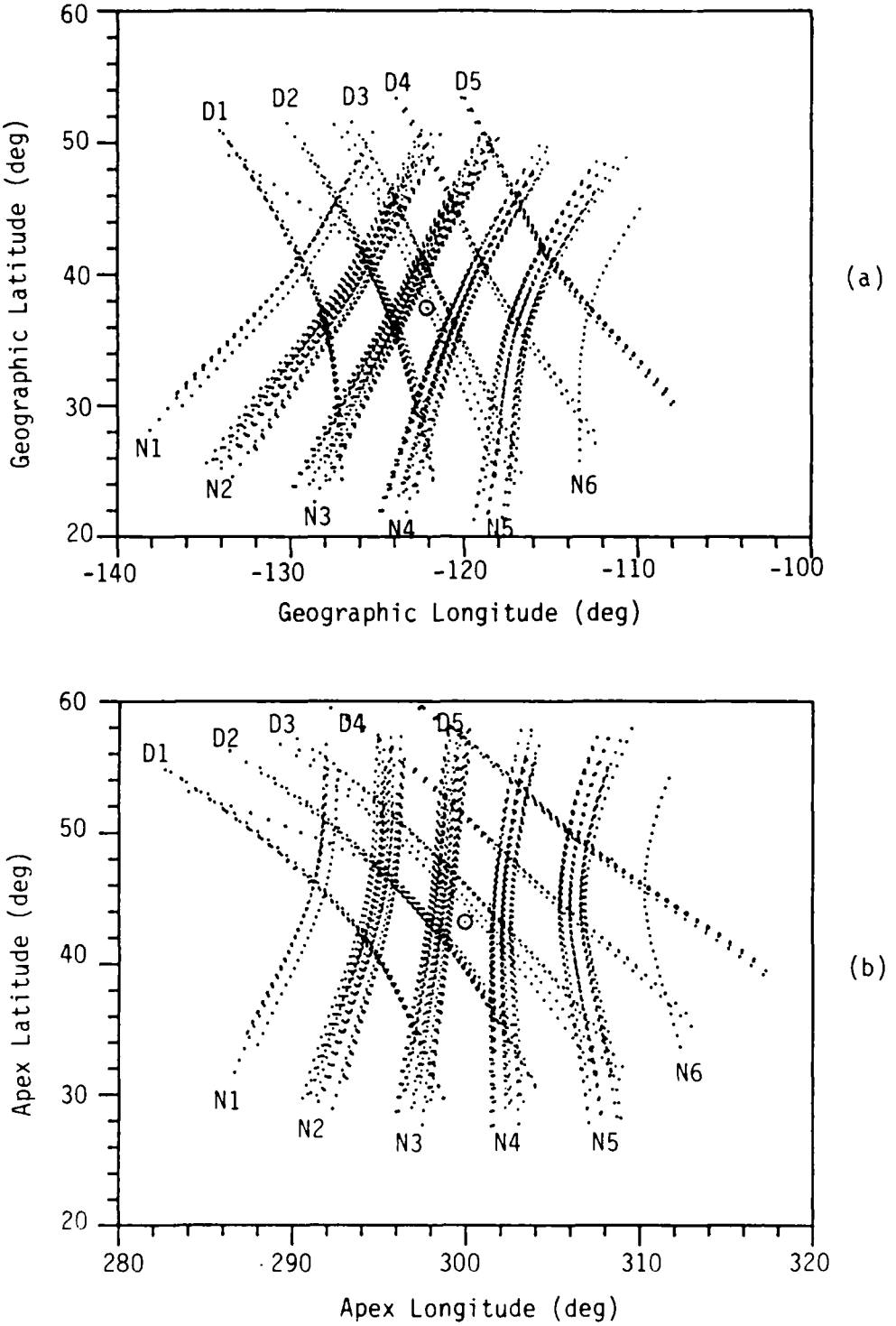

Figure 1. Scatter plots of F-layer (350 km) penetration points from the Stanford Wideband data base. Points are plotted in (a) on a grid of geographic latitude and longitude, and in (b) are on a grid of apex latitude and longitude. In both plots, the receiver location is shown as a small circle. Penetration points fell into six nighttime (N1, N2,...N6) and five daytime (D1, D2,...D5) corridors. Nighttime passes traversed from north to south and daytime passes from south to north.

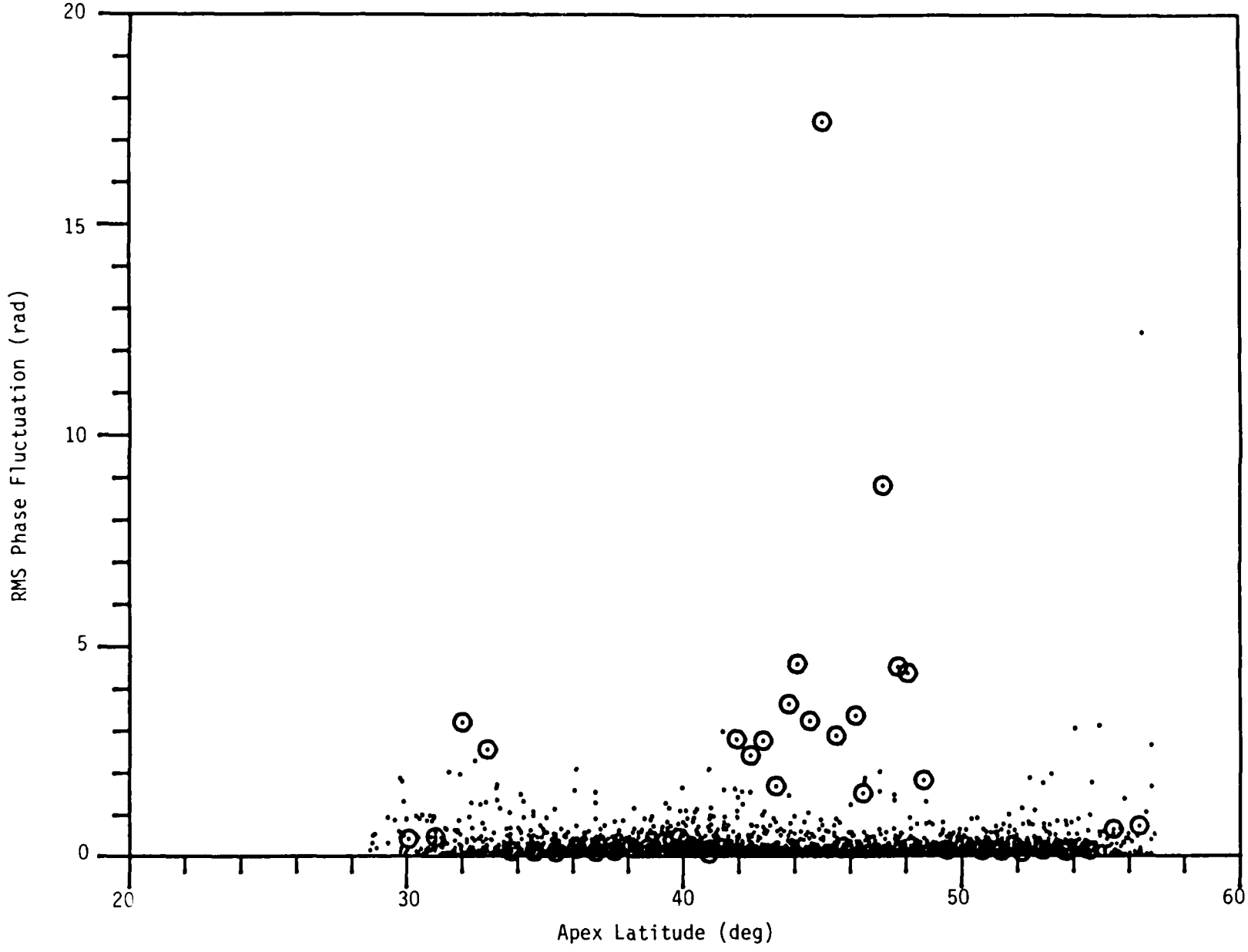

Figure 2. Scatter plots of rms phase fluctuation, σ_ϕ, vs apex latitude, λ_α, for nighttime data from the Stanford Wideband data base. Points from an anomalous pass are shown as small circles

points and 23 daytime passes containing 896 points. In practice, the first and last points of each pass were not used, leaving the actual modeling data base with 2325 nighttime and 850 daytime points.

2.2 BELLEVUE DATA.

When at Bellevue, the HiLat transportable receiver, "Rover," is located at 47°36.5'N and 122°11.5'W (53.45°N, 296.35°E apex latitude and longitude). The data used in this report were collected from 16 April 1984 through 19 April 1986, with a ten-week break from 24 August through 3 November 1984 when Rover was deployed to Hanscom AFB, MA. Although Rover typically locks to HiLat's signals within a few degrees above the horizon, routine processing of beacon data begins at 10° elevation, and the first and last data points so obtained were ignored in our analysis. Figures 3(a) and 3(b) illustrate the coverage provided at Bellevue by HiLat during this period. Both are scatter plots of the apex latitude and longitude of the F-layer penetration point (350km altitude), Figure 3(a) showing coverage in the daytime sector (0800-1600 MLT) and Figure 3(b) showing coverage in the nighttime sector (2000-0400 MLT). Ascending passes on these plots are roughly parallel to the magnetic meridian and descending passes are roughly at 45° to the magnetic meridian.

The magnetic local-time (defined in the apex coordinate system) coverage is illustrated in Figures 4(a) and 4(b). Figure 4(a) is a scatter plot of apex latitude and magnetic local time for the entire data set. As can be seen, all local times are well (and reasonably evenly) sampled. HiLat was able to sample all local times due to precession of its orbit. The effect of this can be seen in Figure 4(b), a scatter plot of apex local time *vs* day-of-year. The broad streaks in this figure are descending passes and the dots are ascending passes. As can be seen, each magnetic local time has been sampled eight times and each season has been sampled four times (with the exception of the period when the receiver was at Hanscom AFB). The entire Bellevue data base for this period contains 27,780 data points from 1304 passes.

A subset of this data base was used for the modeling described in this report. In order to remove any auroral effects from the data base to allow us to focus on mid-latitude behavior, only those data points below apex latitude 54° and having $K_p \leq 5$ were used. This selection reduced the number of points to 3146 points from 774 passes. (Note: Roughly six weeks of observations also were removed due to a cutoff at 28 February 1986 in the available data base on planetary magnetic activity index, K_p,

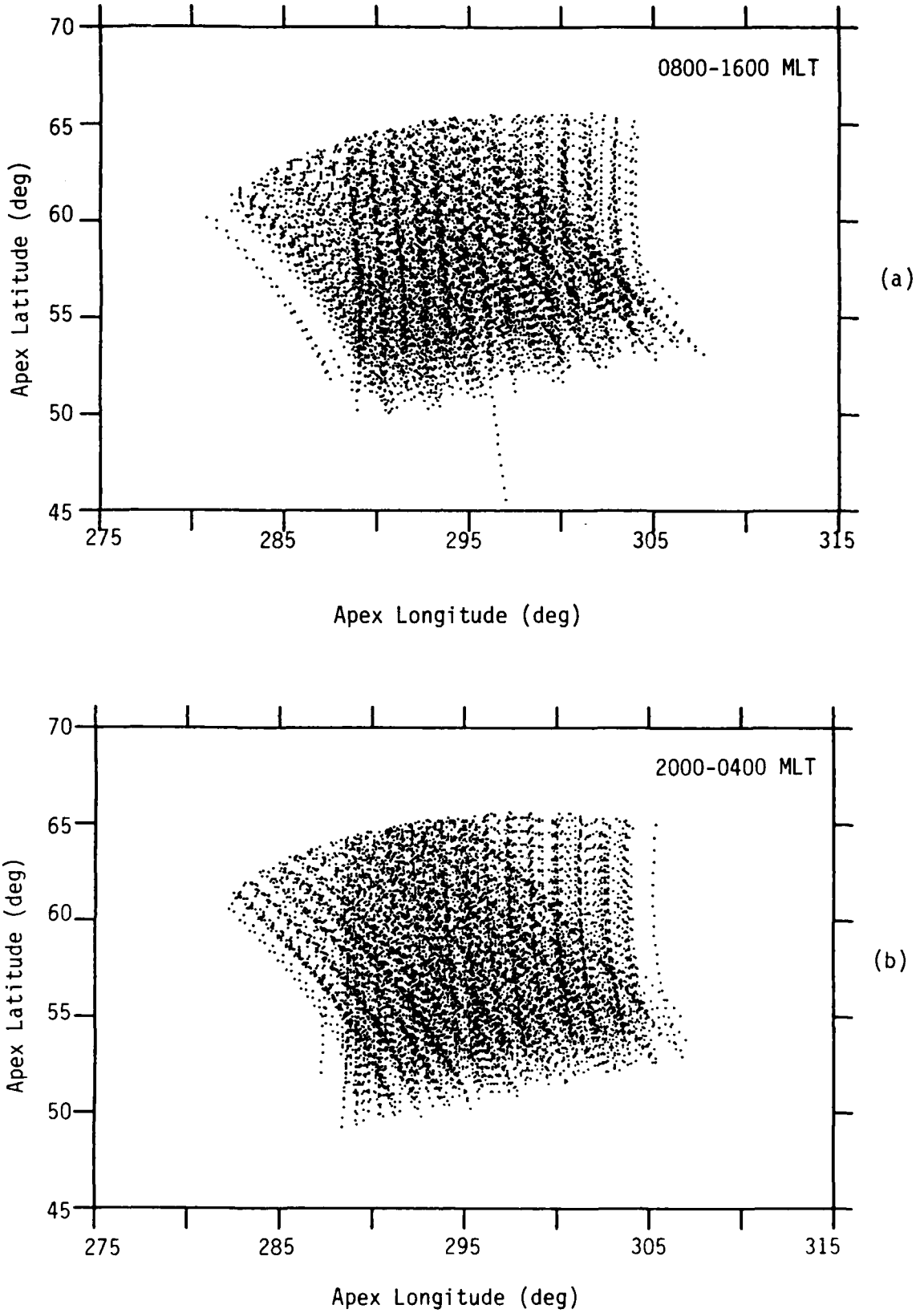

Figure 3. Scatter plots of F-layer (350 km) penetration points from the Bellevue HiLat data base for (a) 0800-1600 apex local time and (b) 2000-0400 apex local time. Points are plotted on a grid of apex latitude and apex longitude.

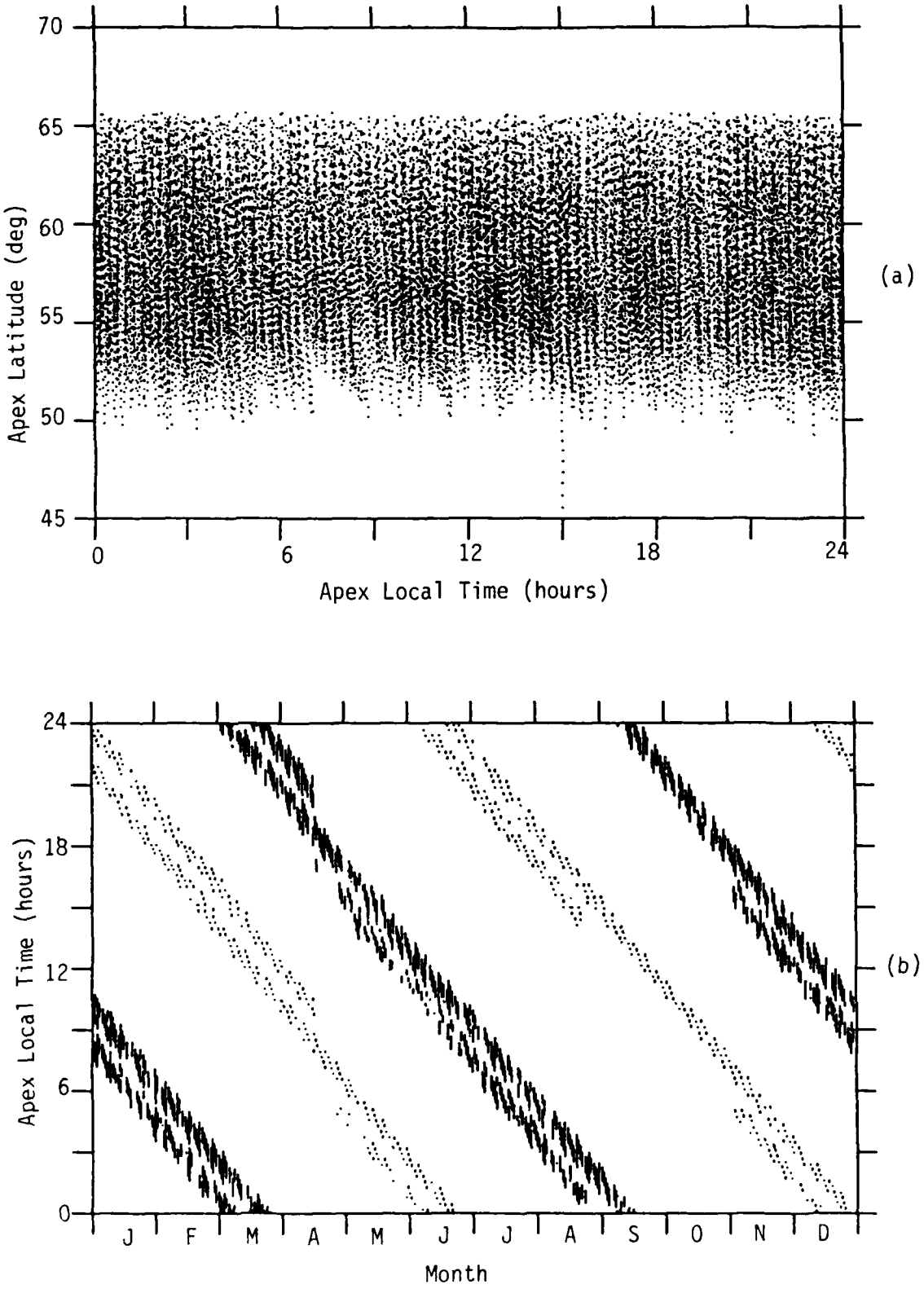

Figure 4. Scatter plots from Bellevue HiLat data base of (a) apex latitude vs. apex local time and (b) apex local time vs. day of year.

and raw sunspot number, SSN.) The effect of this reduction on the overall magnetic local time coverage was minimal, as can be seen from Figure 5, which is a repeat of Figure 4(b) for the reduced data set.

As the modeling procedures used to specify the behavior of C_kL require an assumption that the variations of C_kL with time, season, K_p, and SSN are independent of one another, several scatter plots were generated to check for inadvertent correlations between these parameters, which could bias the modeling results. Figures 6(a) through 6(e), scatter plots of K_p with day of year, SSN with day of year, K_p with magnetic local time, SSN with magnetic local time, and K_p with SSN, show that there was, for the most part, little correlated variation between these various parameters.

The strongest correlation found was in the relationship between SSN and day of year (Figure 6(b)), which shows a distinct peak in the early summer due to high SSN values at the start of the HiLat observations in 1984. In order to separate and distinguish between SSN and seasonal variations, our strategy was to remove the SSN variation from C_kL prior to any seasonal modeling. In fact, as shown in Section 4.2.3, there is no further seasonal variation once the SSN variation is accounted for.

2.3 REVIEW OF MODELING PROCEDURE.

In the report on equatorial modeling, an idealized procedure was described for determining the following irregularity parameters: $\vec{V}_d$ (horizontal vector drift velocity of the irregularities), b (cross-field axial ratio), δ(sheet orientation angle), a (field-aligned axial ratio), q (*in-situ* spectral index), h (effective phase-screen height), and C_sL (now changed to C_kL). These parameters were to be determined from the following observables: $\vec{V}_p$ (diffraction-pattern velocity derivable from interferometer measurements), $\rho(x,y)$ (ground measured spatial autocorrelation function - also derivable from interferometer measurements), geometrical enhancement, p (observed phase spectral index), S_4/σ_ϕ (where S_4 is the normalized standard deviation of intensity and σ_ϕ is the standard deviation of phase), and σ_ϕ. Table 1, repeated from the previous report, summarizes the idealized procedure.

For the mid-latitude case, the same approach is applicable, but as in the equatorial case, we have departed from the idealized procedure. Our actual approach is outlined in Table 2, the elements of which are discussed in Sections 3 and 4.

One other parameter, α, the outer scale of scintillation-producing ionospheric irregularities, is required by the model but is not obtainable from scintillation measurements. We have followed our past practice (Fremouw and Lansinger, 1981; Secan

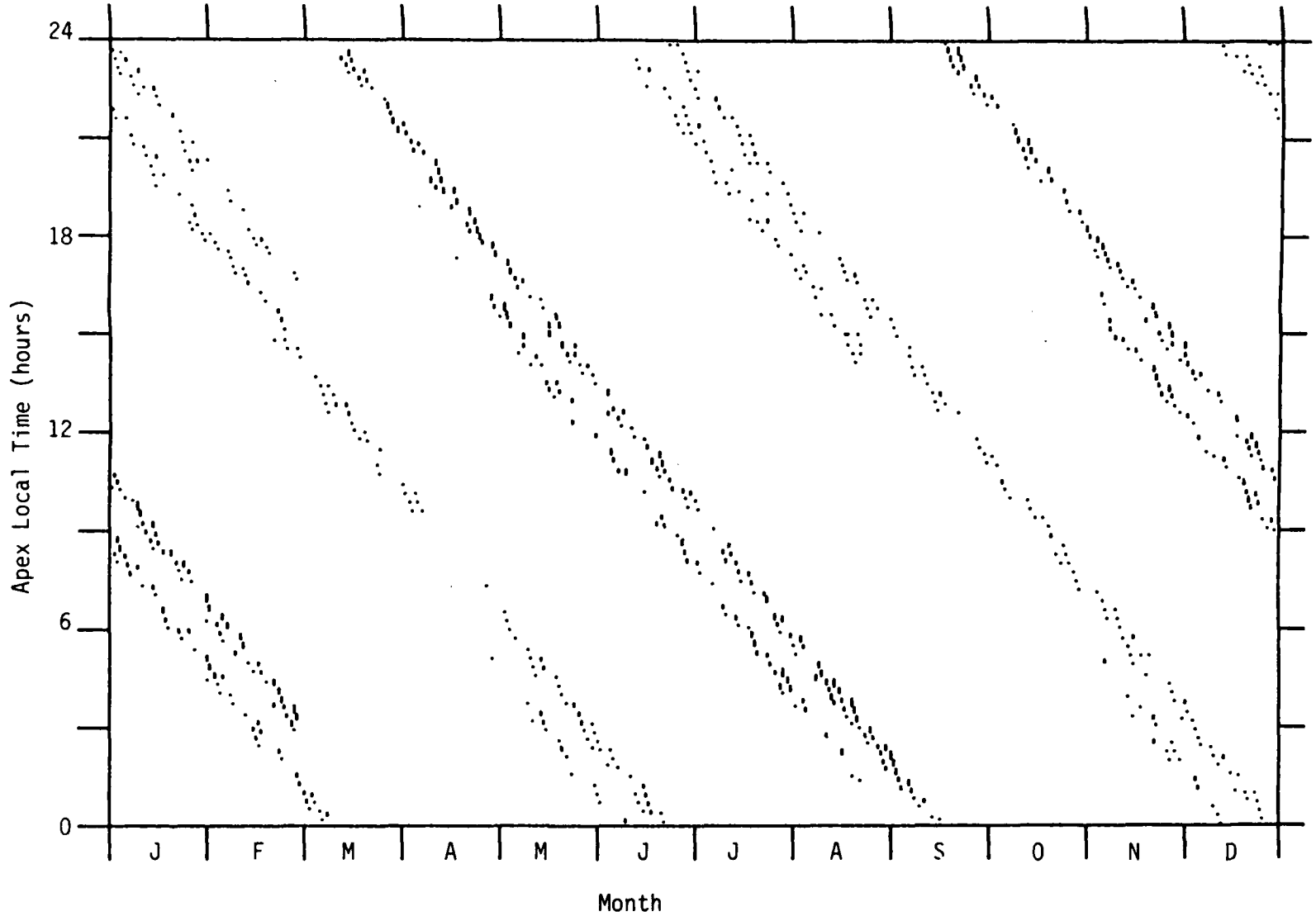

Figure 5. Scatter plot from Bellevue HiLat mid-latitude data base (apex latitude ≤ 54° and K_p<5) of apex local time *vs.* day of year.

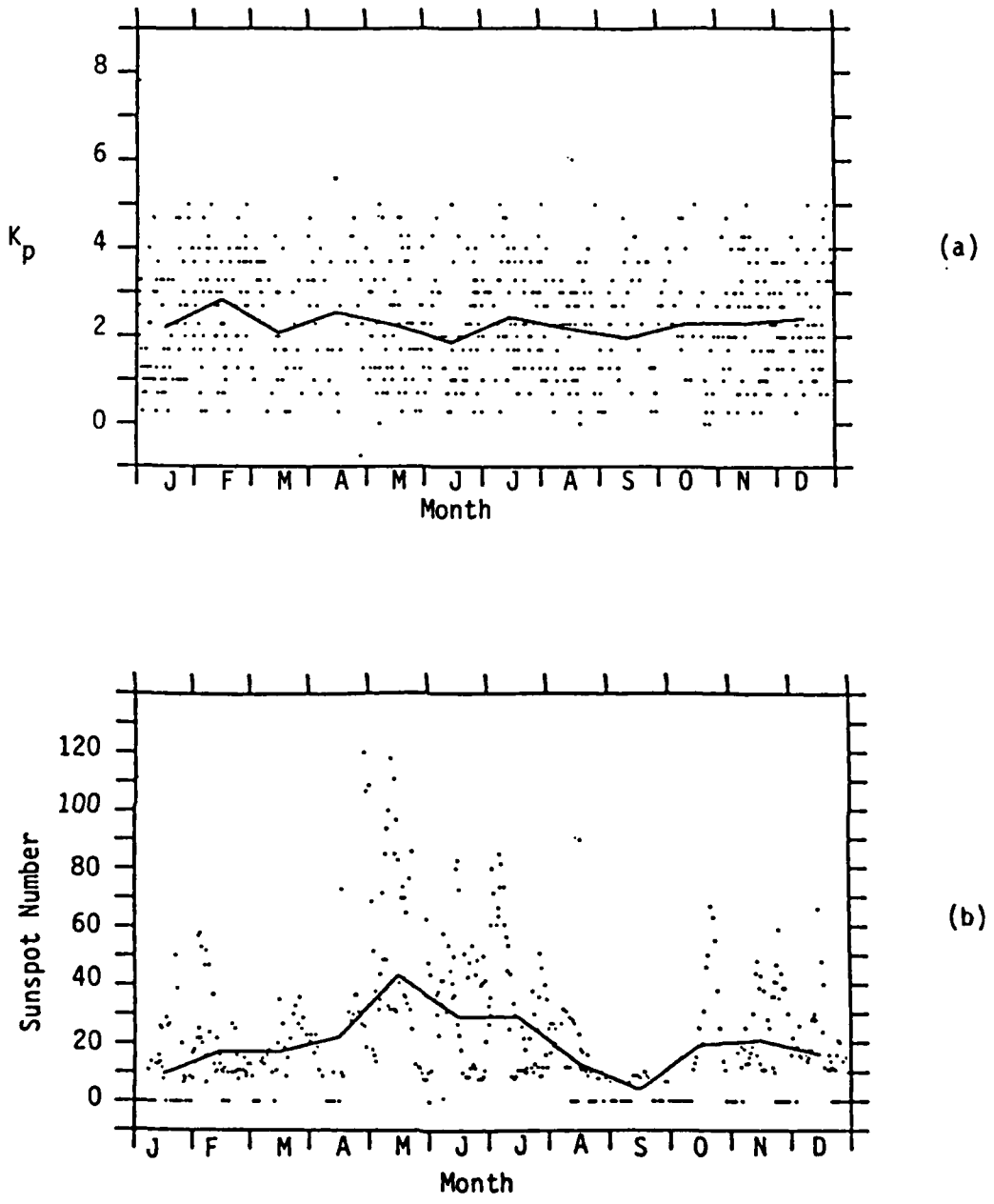

Figure 6. Scatter plots from Bellevue HiLat mid-latitude data base with bin-average plots superimposed: (a) K_p vs. day of year, demonstrating the lack of K_p dependence on season; (b) Sunspot number vs. day of year, exhibiting a peak which implies a possible coupling of the plotted variables; (c) K_p vs. apex local time, demonstrating the lack of K_p dependence on local time; (d) Sunspot number vs. apex local time, demonstrating that sunspot number does not depend on apex local time; (e) K_p vs. sunspot number, demonstrating that K_p does not depend on sunspot number.

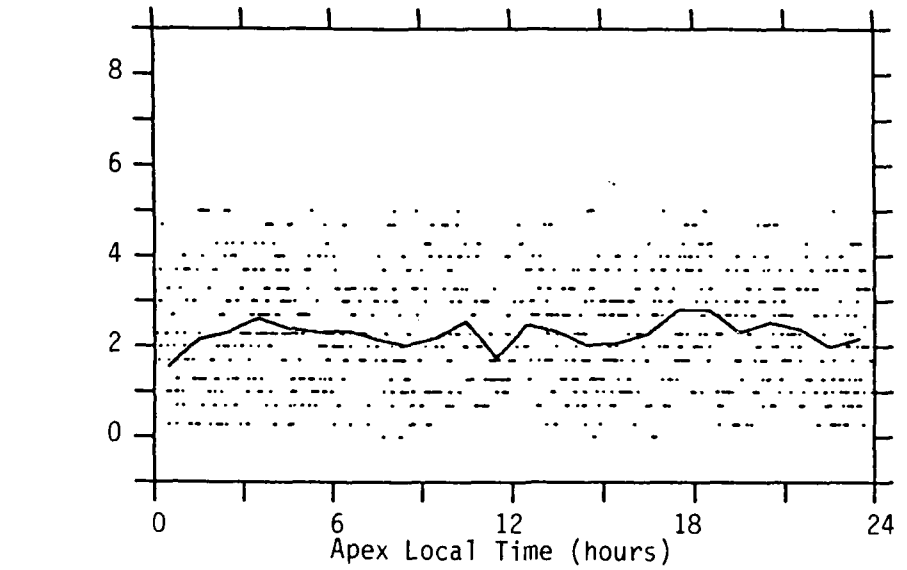

(c)

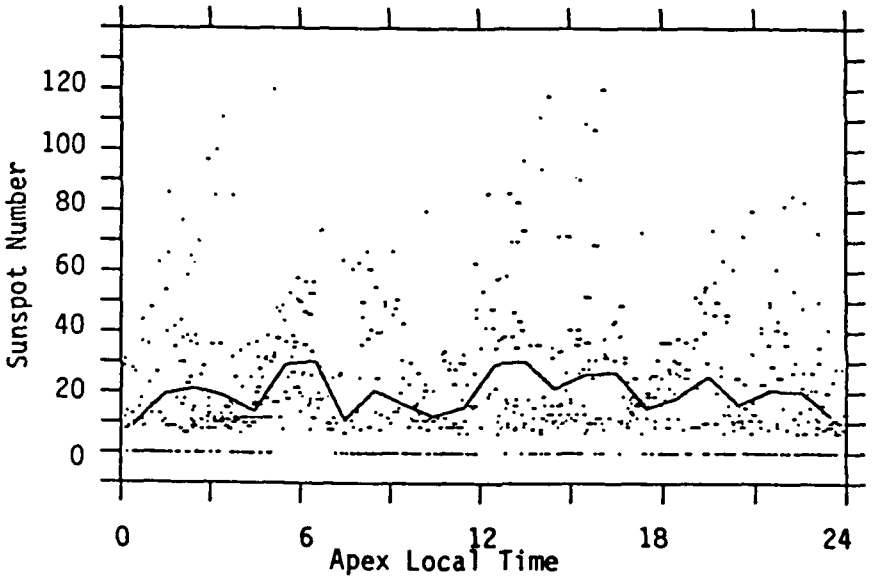

(d)

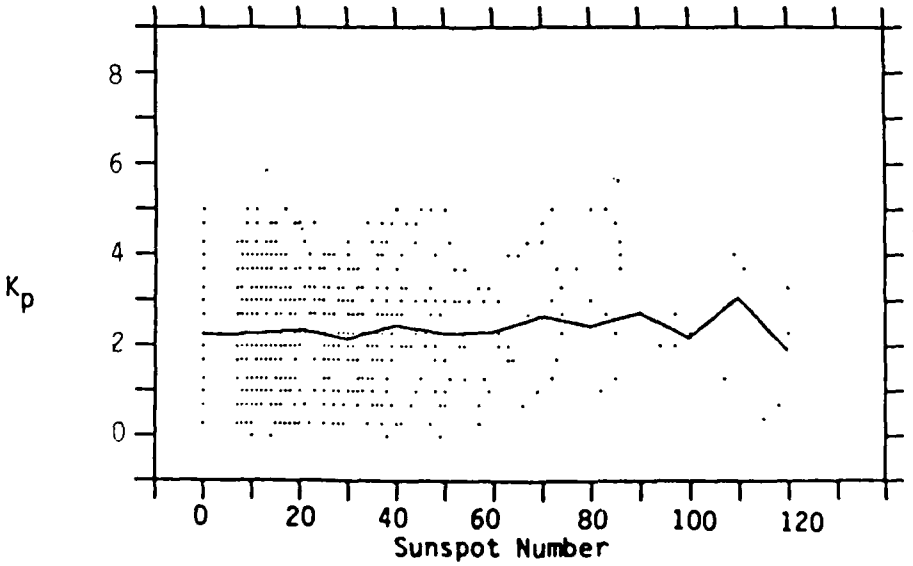

(e)

Figure 6. Scatter plots from Bellevue Hilat mid-latitude data base with bin-average plots superimposed (Concluded).

Table 1. Idealized analysis procedure.

Observables	Physical Parameters: $\vec{V}_d$	δ	b	a	q	h	$C_k L$
Interferometer Measurements: $\vec{V}_d$	X						
Interferometer Measurements: $\rho(x,y)$		X	X	X			
Geometrical Enhancement		X	X	X			
p					X		
S_4/σ_ϕ						X	
σ_ϕ							X

Table 2. Actual analysis procedure.

Observables	Physical Parameters: $\vec{V}_d$	b	δ	a	q	h	$C_k L$
Richmond *et al* (1980)	night:east 20 m/s day:west 20 m/s						
No Extended Enhancement		1	(0)				
Sinno and Minakoshi (1983)				10			
Default					1.5		
S_4/σ_ϕ						350 km	
σ_ϕ							Model

and Fremouw, 1983a; and Fremouw and Robins, 1985) of setting to a large constant value, 1000 km. This value can be overridden by users of WBMOD, and it should soon be refinable by analysis of *in-situ* measurements in the DNA high-altitude effects community.

SECTION 3

DRIFT, SHAPE FACTORS, AND HEIGHT

3.1 DRIFT VELOCITY.

As in the case of the equatorial scintillation model, lack of interferometer results from Wideband led us to deviate from the idealized procedure outlined in Table 1 and to devise a model for convective drift of F-layer irregularities from published incoherent-scatter radar observations.

After reviewing the recent literature, we chose the work of Richmond *et al* (1980) as the basis for WBMOD's description of mid-latitude F-layer drift. Richmond *et al* present results from an empirically calibrated pseudo-electrostatic potential model. The measurements underlying their model are from the facilities at Millstone Hill, St. Santin, Arecibo, and Jicamarca. For V_{dy}, the eastward component of $\vec{V}_d$, we chose a close approximation to the published results at 40°N apex latitude, namely the diurnally cyclic variation,

$$V_{dy} = 20 \sin[(t - 13)\ 2\ /24] \qquad (2)$$

where t is magnetic local time. The other components of $\vec{V}_d$, V_{dx} and V_{dz}, were set to zero.

Transition to the equatorial drift model is provided by means of an error function centered at 20° apex latitude. Transition to the auroral drift model is established by means of an error function centered at the apex latitude of the high-latitude scintillation boundary,

$$\lambda_b = 71.8 - 1.5\ K_p - 5.5 \cos\ (t - 2)\ 2\pi/24, \qquad (3)$$

where K_p is the standard 3-hour planetary magnetic activity index.

3.2 CROSS-FIELD ISOTROPY.

To determine the cross-field axial ratio, b, and the orientation angle, δ, we again followed the example of the equatorial model. As in the case of the data from Ancon and Kwajalein, we observed no extended enhancement along the intersection of any plane with the F layer. We thus set the axial ratio, b, to unity, and the (now inconsequential) orientation angle, δ, to zero. Transition to the auroral value of b again is provided by an error function centered at the high-latitude scintillation boundary. Since the equatorial value of b also is unity and the auroral and equatorial values of δ also are zero, no transitions are needed for these values.

3.3 ALONG-FIELD AXIAL RATIO.

To determine a value for the along-field axial ratio, a, we turned to the work of Sinno and Minakoshi (1983). In their paper, the authors present a study of the effect of geometrical enhancement on the scintillation of VHF signals received at five locations in Japan from the geostationary satellite ETS-II. The five receiver stations provide a range of 0.6° to 17.0° for the angle, ψ_{BP}, between the radiowave propagation vector and the geomagnetic field. The data exhibit increasing scintillation (as measured by the S_4 index) for decreasing ψ_{BP}, and hence demonstrate that geometrical enhancement (which should maximize for $\psi_{BP} = 0$) does in fact produce increased scintillation. Furthermore, Sinno and Minakoshi show that the data agree quite well with theoretical S_4 *vs* ψ_{BP} curves computed for an along-field axial ratio, a, of 10. We therefore selected 10 as the WBMOD mid-latitude value of a. Transition to equatorial and auroral values of a are treated as for drift velocity (see Section 3.1).

3.4 SPECTRAL INDEX.

Although spectral information was not computed for the Wideband Stanford data, the indication from the HiLat Bellevue data was that the mid-latitude value of the spectral index, q, is about 1.85 (see Appendix B). This result was somewhat surprising since examination of the equatorial and auroral Wideband data had led in each case to a choice of 1.5 for q. As discussed in Appendix B, it appears that Wideband-*vs*-HiLat processing differences are at least partially responsible for this observed difference. Suggestive though the Bellevue results may be, we have decided for the time being to set the mid-latitude value of q to 1.5, the equatorial and auroral value, pending completion of our examination of the processing and geophysical influences on measured spectral index.

3.5 HEIGHT OF THE EQUIVALENT PHASE SCREEN.

With the irregularity shape parameters, a, b, and [illegible], set, we were able to determine the equivalent phase-screen height, h, from values of the ratio S_4/σ_ψ (where S_4 is the standard deviation of intensity normalized by the mean intensity and σ_ψ is the standard deviation of phase). Figure 7(a) shows plots of average S_4/σ_ψ *vs* λ_a for the entire Stanford data base. The solid line is for the observed values, and the dashed lines are for point-by-point simulations of the data base using choices for the equivalent phase screen height, h, of 250, 350, and 450 km. The simulations were done

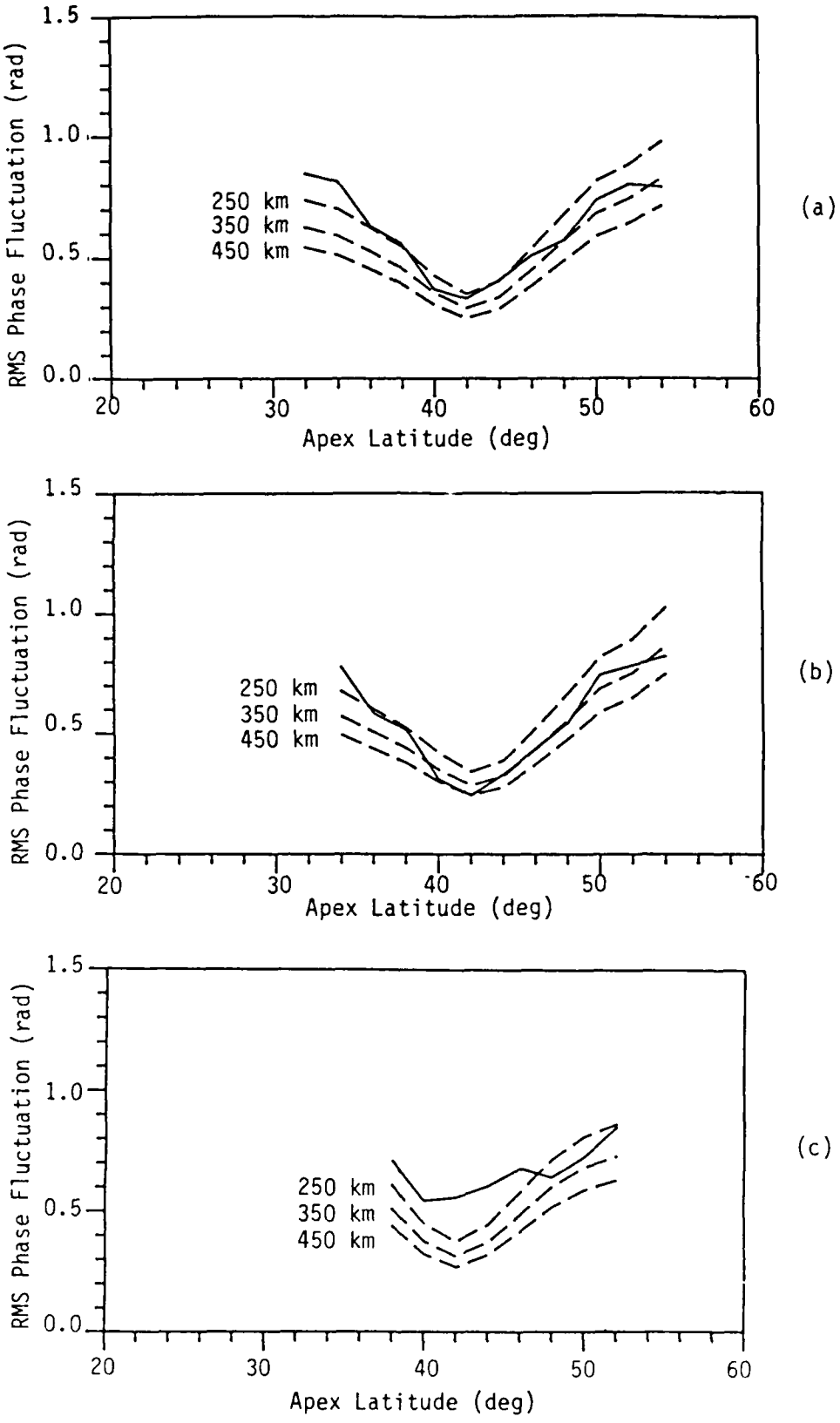

Figure 7. Bin-average plots of the ratio of intensity scintillation index, S_4, to phase scintillation index, σ_ϕ, vs apex latitude, for Stanford observations (solid lines) and WBMOD simulations (dashed lines). Simulation results are shown for phase-screen heights of 250, 350, and 450 km. Figures 7(a), 7(b) and 7(c) are for night and day, night only, and day only, respectively. Latitude bins are 2° wide, and bins containing fewer than 100 points for (a) and (b) and 50 points for (c) are not shown.

with a modified version of WBMOD, using the parameter choices described in the previous sections.

Figure 7(a) suggests that a reasonable choice for h lies in the range 250 to 350 km. Figures 7(b)and 7(c) show nighttime and daytime data, respectively, and are otherwise identical to Figure 7(a). Figure 7(b) suggests a choice for h of about 350 km, but Figure 7(c) indicates a value for h of less than 250 km. The latter indication suggests that the E layer is an important contributor to overall observed daytime scintillation. Since WBMOD is a model of F-layer-produced scintillation, we are guided by the nighttime results to choose the WBMOD mid-latitude value of h to be 350 km, the same value selected for equatorial and auroral regions.

SECTION 4

IRREGULARITY STRENGTH MODEL

4.1 PROCEDURE.

In the previous sections we have described the determination of all parameters in the mid-latitude scintillation model except for the height-integrated strength of irregularities, the modeling of which is described in this section. In previous versions of WBMOD the irregularity strength for equatorial and auroral regions has been modeled in terms of the quantity $\sqrt{C_s L}$. For reasons explained in Appendix A, we are changing from $C_s L$ to the quantity $C_k L$. $C_k L$ is given by equation (1) which we repeat here:

$$C_k L = \left(\frac{1000}{2\pi} \text{ meters}\right)^{1+p} C_s L$$

where p is the phase spectral index. We have further decided, for reasons explained below, actually to model the quantity $\log \sqrt{C_k L}$.

Figures 8(a) and 8(b) show histograms of $\sqrt{C_k L}$ and $\log \sqrt{C_k L}$, respectively, for the Bellevue HiLat database. The distribution of $\log \sqrt{C_k L}$ is approximately normal, while the $\sqrt{C_k L}$ distribution is strongly skewed. We have thus decided to model $\log \sqrt{C_k L}$ rather than $\sqrt{C_k L}$ in order to take advantage of the desirable statistical properties of normally distributed data.

Our basic assumption regarding the quantity $\log \sqrt{C_k L}$ is that it can be represented as the sum,

$$\log \sqrt{C_k L} = C + f_{\cdot}(\cdot_a) + f_T(t) + f_R(R) \qquad (4)$$

where C is a lead constant, and $f_{\cdot}$, f_T and f_R are functions depending respectively on the apex latitude $\cdot_a$, the magnetic (apex) local time t (hours), and R, the sunspot number.

Data bases of $\log \sqrt{C_k L}$ values were obtained for Stanford (from $\cdot$) and Bellevue (from T and p), using the relations described in Appendix A. We then used the Stanford data to find the functional form for $f_{\cdot}$, the Bellevue data to find the forms for f_T and f_R, and finally, the Stanford data for the value of C. It is worth noting that even though we have set the model value of the *in-situ* spectral index, q, to 1.5, we have

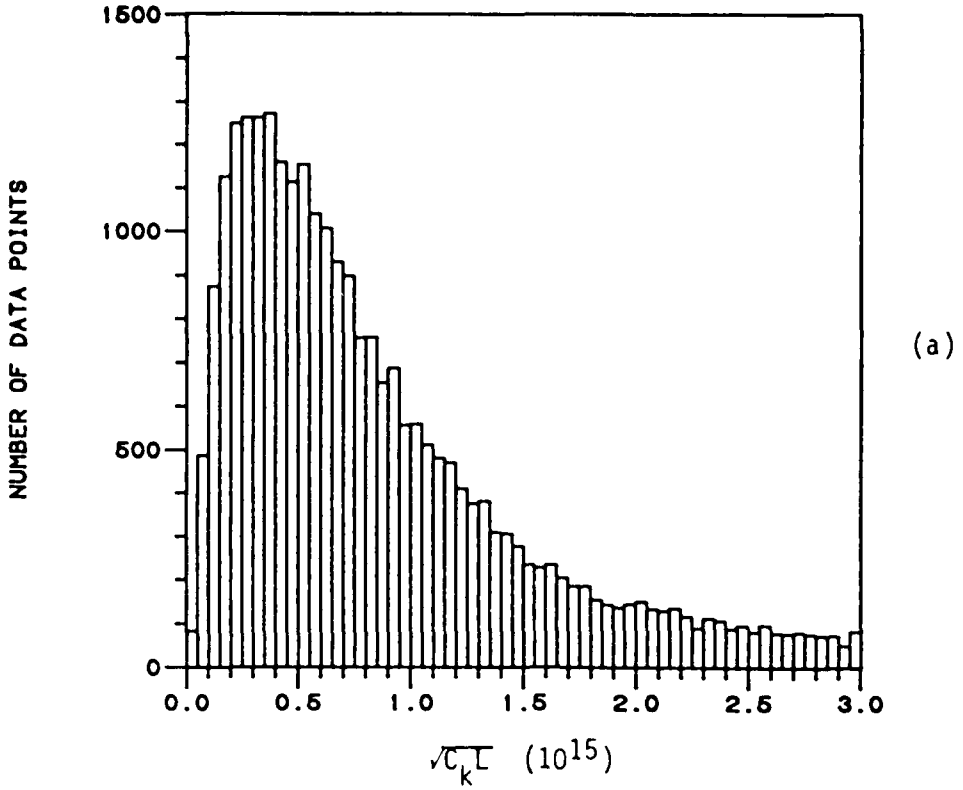

(a)

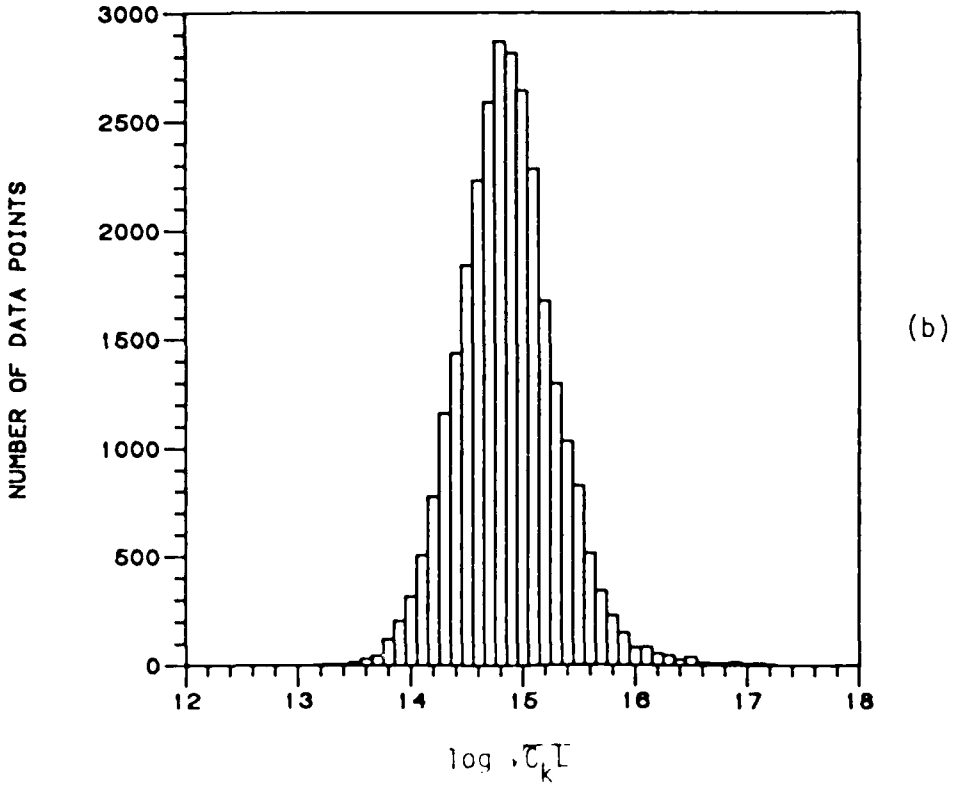

(b)

Figure 8. Histograms of (a) $\sqrt{C_k L}$ data and (b) log $\sqrt{C_k L}$ data for the Bellevue HiLat data base.

used the measured phase spectral index p = 2.85 for the purpose of computing the mid-latitude irregularity strength for the Bellevue data. (See Appendix B.)

4.2 RESULTS.

The significant details in our determination of the three functions and the lead constant in the representation for log $\sqrt{C_k L}$ will now be described.

4.2.1 Latitudinal Variation.

Shown in Figures 9(a) and 9(b) are scatter plots of log $\sqrt{C_k L}$ vs λ_a with line plots of bin-averaged log $\sqrt{C_k L}$ vs λ_a superimposed, for the Stanford Wideband data base. Figure 9(a) shows nighttime, and Figure 9(b) shows daytime data. The Bellevue data base was not used because its latitudinal range did not extend far enough equatorward.

It can be seen from Figures 9(a) and 9(b) that there is an increasing trend in log $\sqrt{C_k L}$ toward the lower and upper extents of the observed λ_a range. Appendix B discusses several aspects of this behavior, including the possibility that the scattering-theory assumption of a thick (with respect to irregularity correlation length) irregularity layer does not hold. At the same time, it is clear that for λ_a in the range of 35° to 45° there is little or no trend in $\sqrt{C_k L}$ as a function of λ_a. Juxtaposing this observation with the uncertainties surrounding the trends in $\sqrt{C_k L}$ for λ_a 35° and λ_a 45°, we have decided to take a conservative approach and set $f_1(\lambda_a)$ to zero. We do, however, need to mesh the mid-latitude model with the equatorial and auroral models. We do so by assuming an error function decay to zero for the mid-latitude contribution as λ_a approaches the equatorial and auroral regions. The half-maximum points of the error functions are set at the equatorial transition point, λ_a = 20°, and at the high-latitude scintillation boundary, λ_b, given by equation (3). The error function decay rates are chosen to match the decay rates of the apex-latitude-dependent terms in the equatorial and auroral scintillation models.

An additional feature in the mid-latitude model is a plasmapause term given by

$$(\sqrt{C_k L})_{pp} = C_{pp} K_p^2 \left(1 + \cos\frac{2\pi t}{24}\right) \exp\left|-\left(\frac{\lambda_a - \lambda_{pp}}{2.5}\right)^2\right| \qquad (5)$$

where C_{pp} is a lead constant, K_p is the magnetic index, t is magnetic (apex) time, λ_a is apex latitude, and λ_{pp} is the plasmapause location given by $\lambda_b - 2.5$, λ_b being the the scintillation boundary given by equation (3). This term is discussed by Fremouw (1984).

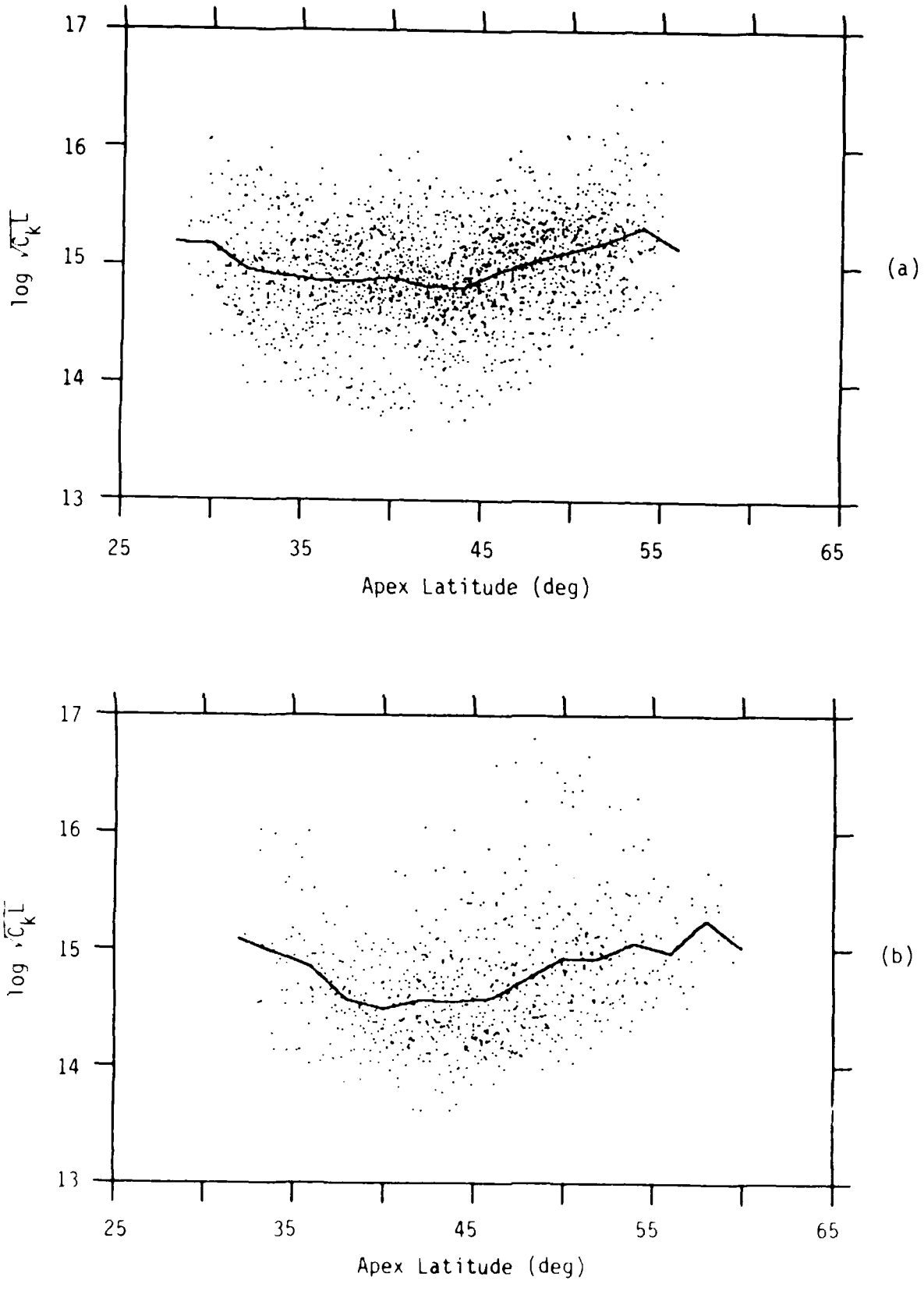

Figure 9. Scatter plots of log $\langle C_k \rangle$ vs apex latitude for the Stanford Wideband (a) nighttime and (b) daytime data bases. Bin-average plots are superimposed.

4.2.2 Diurnal Variation.

Figure 10 shows a scatter plot of log $\sqrt{C_k L}$ vs apex local time from the Bellevue data base for λ_a 54° and $K_p \leq 5$; a line plot of bin-averaged log $\sqrt{C_k L}$ is superimposed (jagged line). We favor the Bellevue data over Stanford for determining the time dependence because the time window for the Stanford data was too narrow, being only 110 minutes at night and 100 minutes during the day. Noting a data maximum near midnight and a minimum near noon, we obtained a best sinusoidal fit (shown by the smooth line in Figure 10) to the Bellevue data, the peak-to-peak amplitude being 0.30. Thus, we set $f_T(t)$ to 0.15 cos $\frac{2\pi t}{24}$. For the Stanford data the difference between the nighttime and daytime averages of log $\sqrt{C_k L}$ is 0.24, which is similar to the Bellevue peak-to-peak value.

4.2.3 Sunspot Number Dependence.

Figure 11 shows a scatter plot of log $\sqrt{C_k L}$ vs sunspot number for the previously defined Bellevue data set with the diurnal variation and the mean log $\sqrt{C_k L}$ subtracted out; a line plot of bin-average log $\sqrt{C_k L}$ is superimposed (jagged line). The slope of a best-fit linear approximation to these data (shown by the straight line in Figure 11) is 0.002, and we have set $f_R(\bar{R})$ to 0.002 $\bar{R}$.

Figure 12 shows a scatter plot of log $\sqrt{C_k L}$ vs day of year (bin-agerage plot and zero level superimposed) after the diurnal and sunspot number dependencies and a mean level are removed from the data. A lack of seasonal dependence is evident, and so the previously observed (Figure 6b) possible coupling between sunspot number and season is of no concern.

4.2.4 $\sqrt{C_k L}$ Lead Constant.

Since our model-vs-data evaluation tests are performed for Stanford data corridors (see Section 5.1), and since the Stanford/Bellevue discrepancy is not completely resolved (see Appendix B), we decided to use the Stanford data to evaluate the lead constant in our model for log $\sqrt{C_k L}$. In the previous sections we have shown that a suitable mid-latitude model for log $\sqrt{C_k L}$ can be written as

$$\log \sqrt{C_k L} = C + 0.15 \cos \frac{2\pi t}{24} + 0.002 R.$$

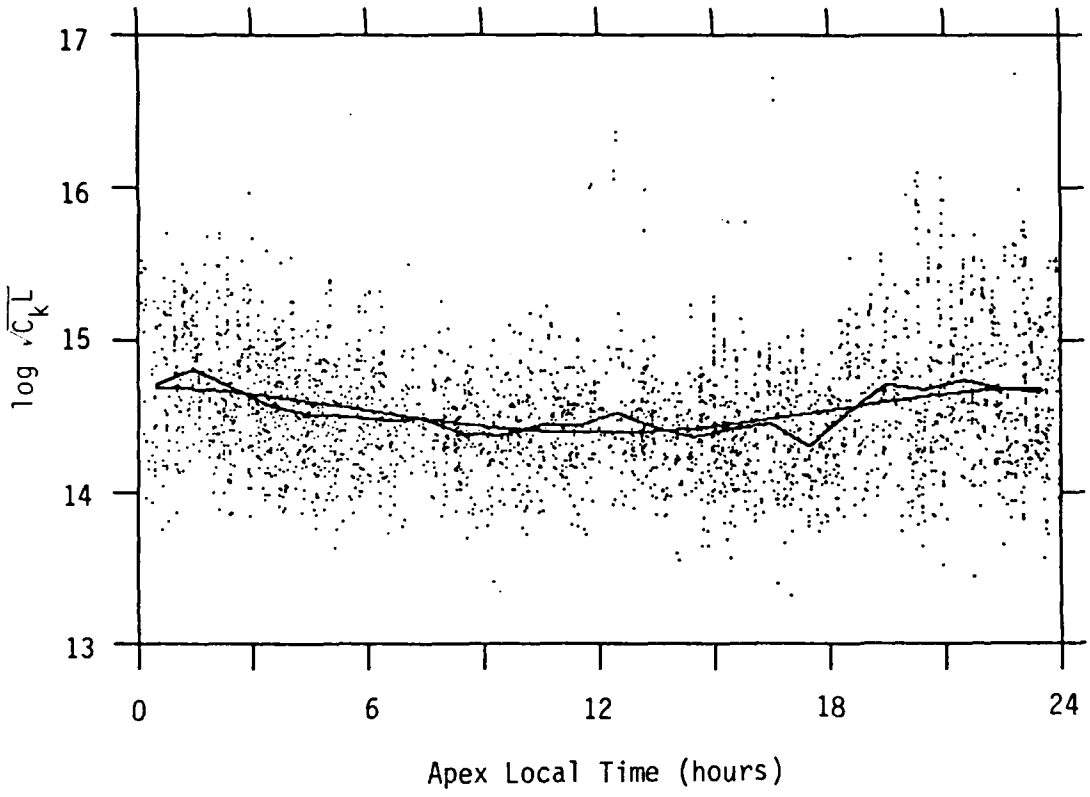

Figure 10. Scatter plot of log $\sqrt{C_k L}$ vs apex local time for the Bellevue HiLat mid-latitude data base. Bin-average (jagged line) and best fit sinusoidal (smooth line) plots are superimposed. The peak to peak amplitude of the sinusoid is 0.30.

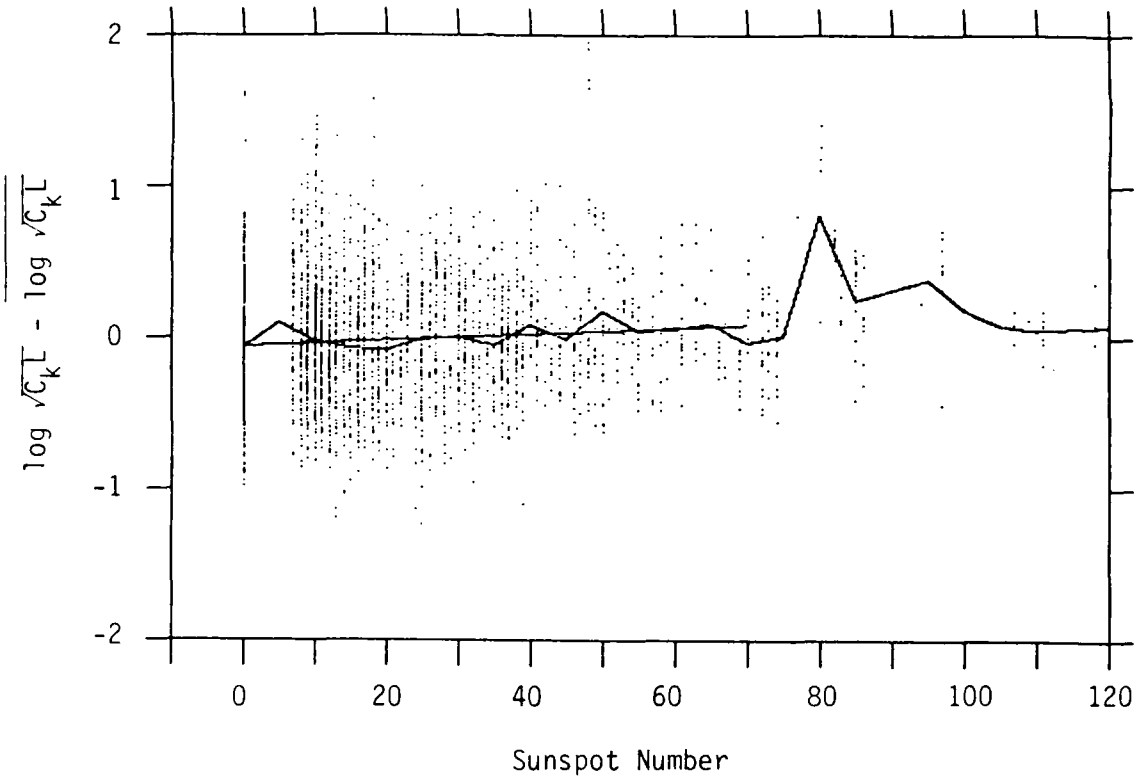

Figure 11. Scatter plot of log $\sqrt{C_k}$ vs sunspot number (SSN) for the Bellevue HiLat mid-latitude data base. The log $\sqrt{C_k}$ mean and the apex local time variation have been subtracted from the log $\sqrt{C_k}$ data. A bin-average plot (jagged line) and a best fit straight line are superimposed. The best fit is computed for the SSN range 0-70.

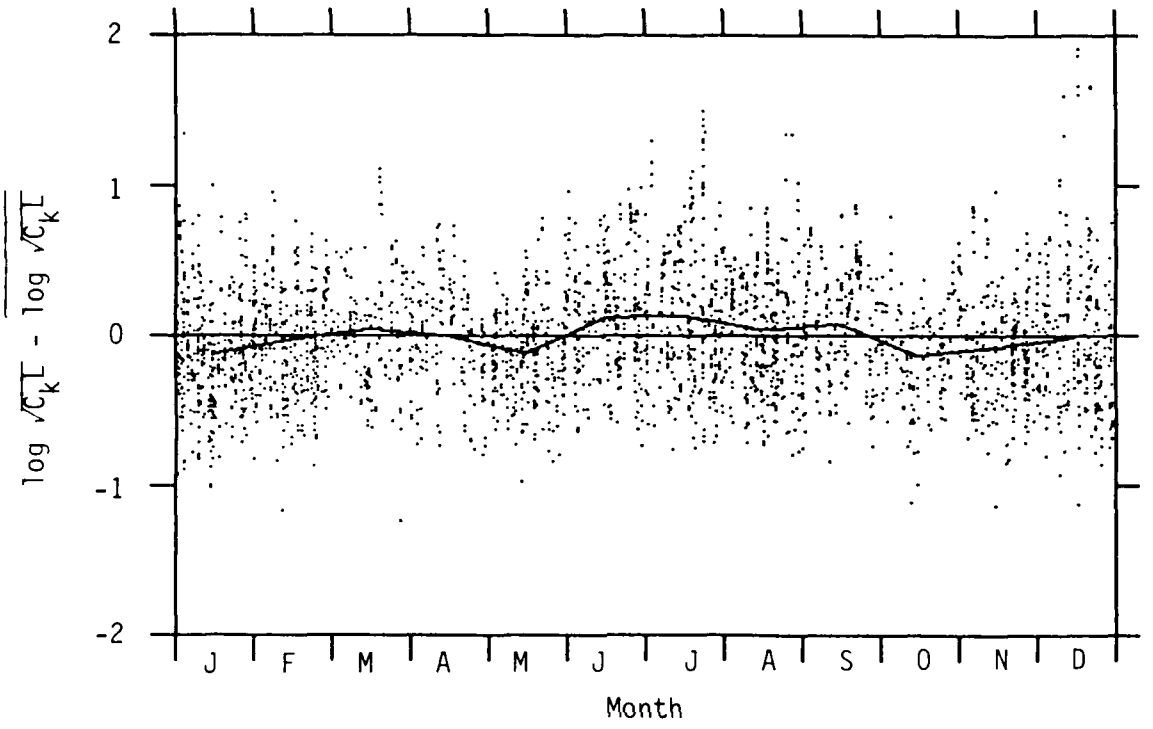

Figure 12. Scatter plot of log $\sqrt{C_k L}$ vs day of year for the Bellevue HiLat mid-latitude data base. A bin-averaged plot and the zero level are superimposed. Subtracted from the log $\sqrt{C_k L}$ data are the log $\sqrt{C_k L}$ mean and the previously computed best fits for apex local time and sunspot number variations. The plot shows the absence of any seasonal variation.

The lead constant can be evaluated by taking averages over the Stanford data base on both sides of this equation. Since it is actually $\sqrt{C_k L}$ that is required by WBMOD to obtain σ_ϕ and S_4, we rewrite the above equation, prior to taking averages, as

$$\sqrt{C_k L} = K\ 10^{0.15 \cos \frac{2\pi t}{24}}\ 10^{0.002R}. \qquad (6)$$

By taking averages on both sides of this equation, we can obtain K, the log of which is the lead constant, C.

Since the Stanford data are not evenly distributed over time of day, we take separate night and day averages. We restrict ourselves to the latitude band $35° \leq \lambda_a \leq 45°$, since it was data from this region that motivated our decision to set $f_\lambda(\lambda_a) = 0$ (see Section 4.2.1). The following table summarizes the results:

Table 3. Night and day means for Stanford data satisfying $35° \leq \lambda_a \leq 45°$.

	$\sqrt{C_k L}$	$10^{0.15 \cos \frac{2\pi t}{24}}$	$10^{0.0002R}$
NIGHT	1.697 E15	1.403	1.0646
DAY	1.090 E15	0.730	1.0617

Treating day and night equally, we obtain

$$\text{mean}\ (\sqrt{C_k L}) = 1.3935\ \text{E15}$$

and $\text{mean}\ (10^{0.002R}) = 1.063.$

We set the diurnal mean of $0.15 \cos \frac{2\pi t}{24}$ to unity, the ideal result for data uniformly distributed in time. It then follows from equation (6) that K is 1.311 E15 and the lead constant C is 15.12.

SECTION 5

CONCLUSION

5.1 EFFICACY OF WBMOD.

The results from the previous sections were incorporated into WBMOD, and evaluation tests of the new mid-latitude scintillation model were performed. Results of model/data comparisons for the Stanford data corridors defined in Figures 1(a) and 1(b) (see Section 2.1) are presented below.

To increase the statistical significance of our results, we found it advantageous to combine certain data corridors. Figures 13(a) through 13(d) show scatter plots of Briggs-Parkin angle, ψ_{BP}, *vs* apex latitude, λ_a, for nighttime data corridors N2, N3, N4, and N5, respectively. It can be seen that the ψ_{BP} *vs* λ_a behavior is similar for N3 and N4, the two more nearly overhead corridors. Namely, for each of these corridors, ψ_{BP} reaches a minimum between 10° and 20° at an apex latitude close to that of the receiver. The scatter plots for corridors N2 and N5 also are qualitatively similar. We therefore grouped corridor N3 with N4 and N2 with N5 for comparisons between model results and data. In a similar manner, Figures 14(a) through 14(e) support the grouping of daytime data corridor D2 with D3 (most nearly overhead), and D1 and D2 with D5.

To perform the model/data comparison presented below, we used a modified version of WBMOD to simulate the satellite geometry and each data point of each pass. Figures 15(a) and (b) show the comparisons for the nighttime data and Figures 16(a) and (b) show the comparisons for the daytime data. Most satisfying is that the geometrical enhancement peaks for both night and day overhead corridor groups are reproduced by WBMOD with reasonable accuracy. For all corridors the model/data agreement for λ_a between 35° and 45° is quite good, as we should expect, since that is where the absence of latitudinal variation in model C_kL is consistent with the lack of latitudinal variation in the C_kL data. North and south of this interval the observed scintillation strength generally exceeds the model results. It is hoped that further observations from HiLat and Polar BEAR will help to explain these trends, at least in the latitude regime for which $\lambda_a \geq 45°$.

5.2 SUMMARY.

From contributions to the literature, the limited data base collected at Stanford during the first four months of the DNA Wideband experiment, and a subset of the

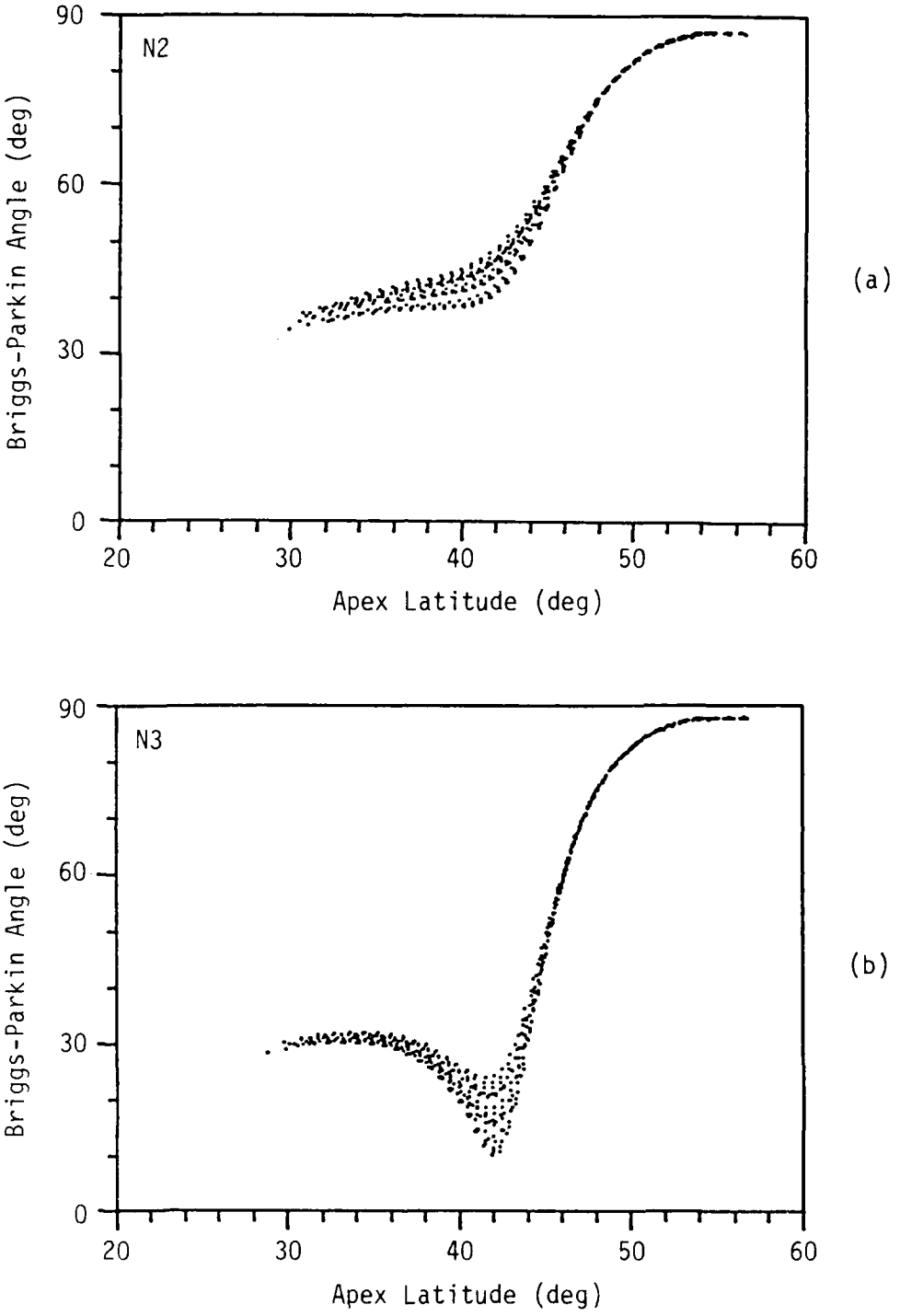

Figure 13. Scatter plots of Briggs-Parkin angle vs magnetic apex latitude, λ_a, for nighttime data corridors N2, N3, N4, and N5. Plots are shown in (a), (b), (c), and (d), respectively.

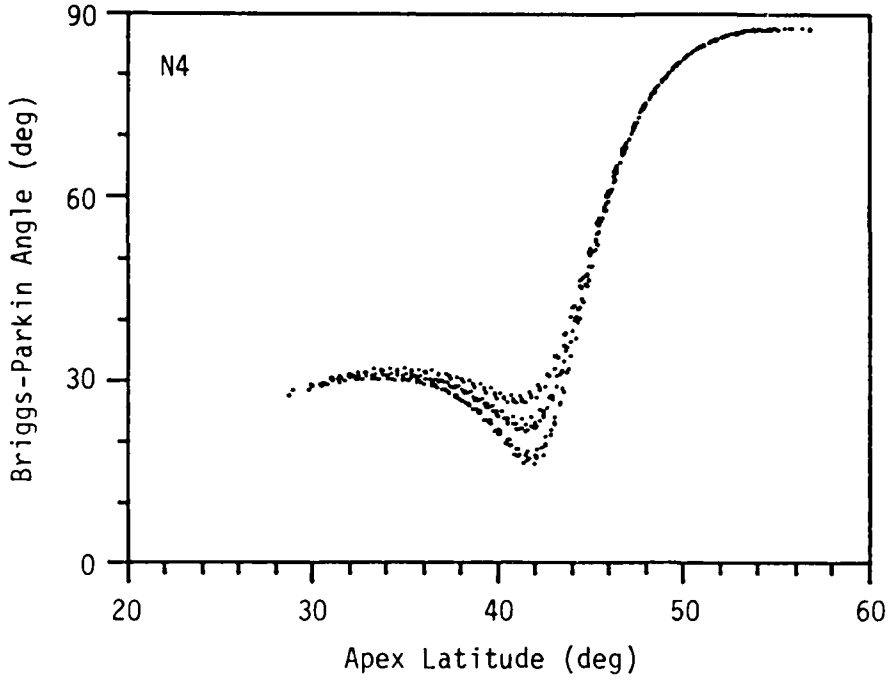

(c)

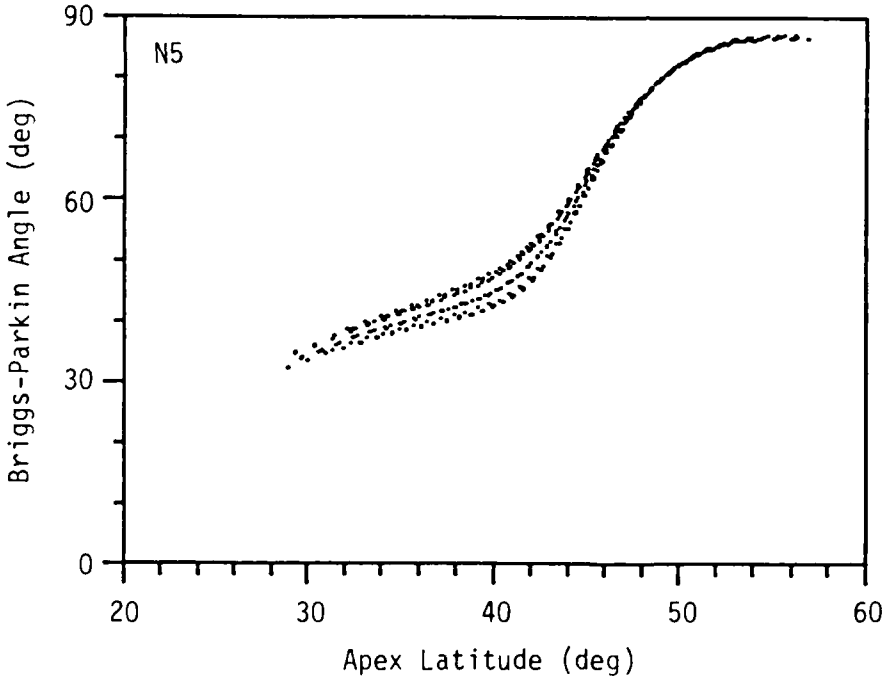

(d)

Figure 13. Scatter plots of Briggs-Parkin angle vs magnetic apex latitude, λ_a, for nighttime data corridors N2, N3, N4, and N5. Plots are shown in (a), (b), (c), and (d), respectively (Concluded).

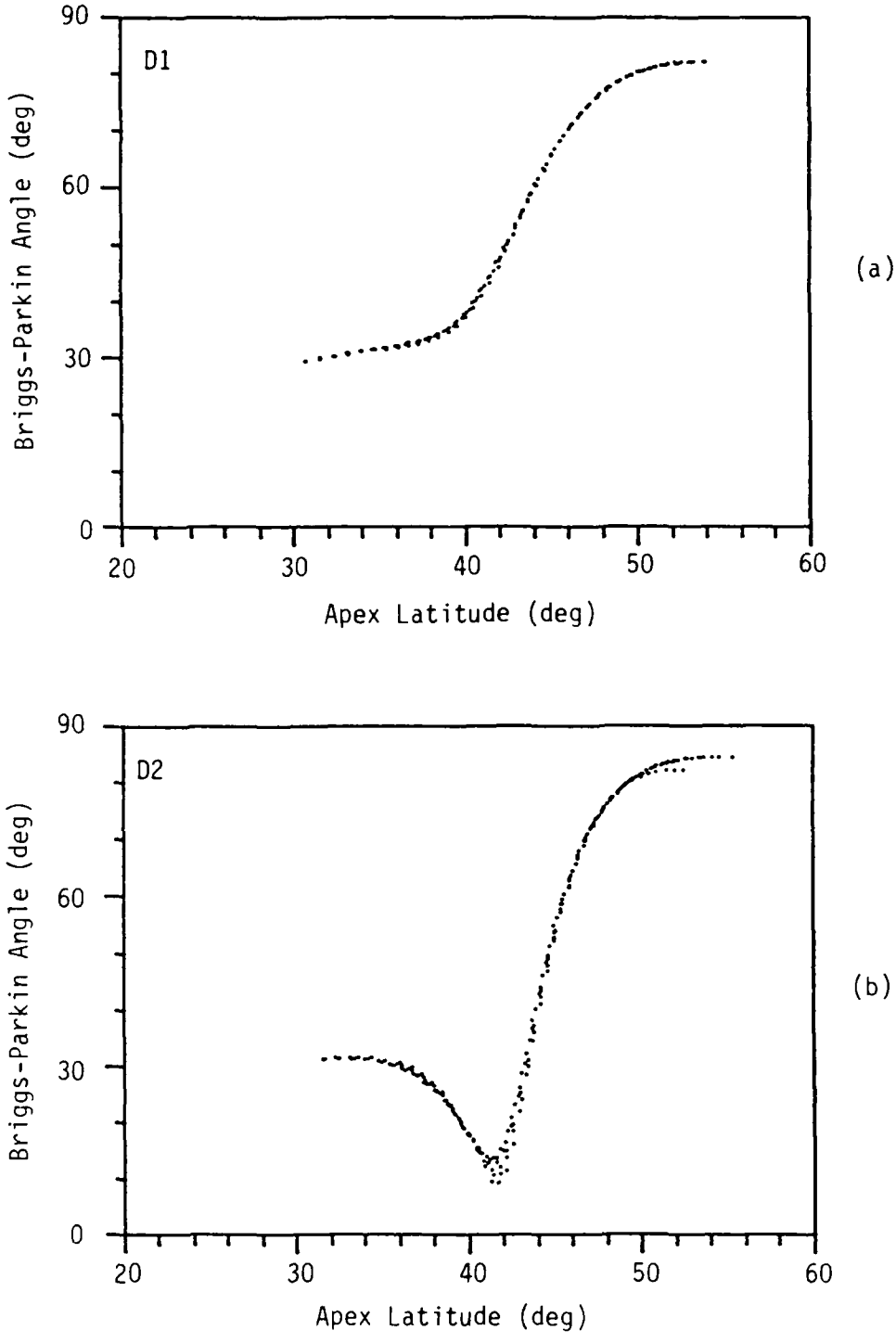

Figure 14. Scatter plots of Briggs-Parkin angle vs magnetic apex latitude, λ_a, for daytime data corridors D1, D2, D3, D4, and D5. Plots are shown in (a), (b), (c), (d), and (e), respectively.

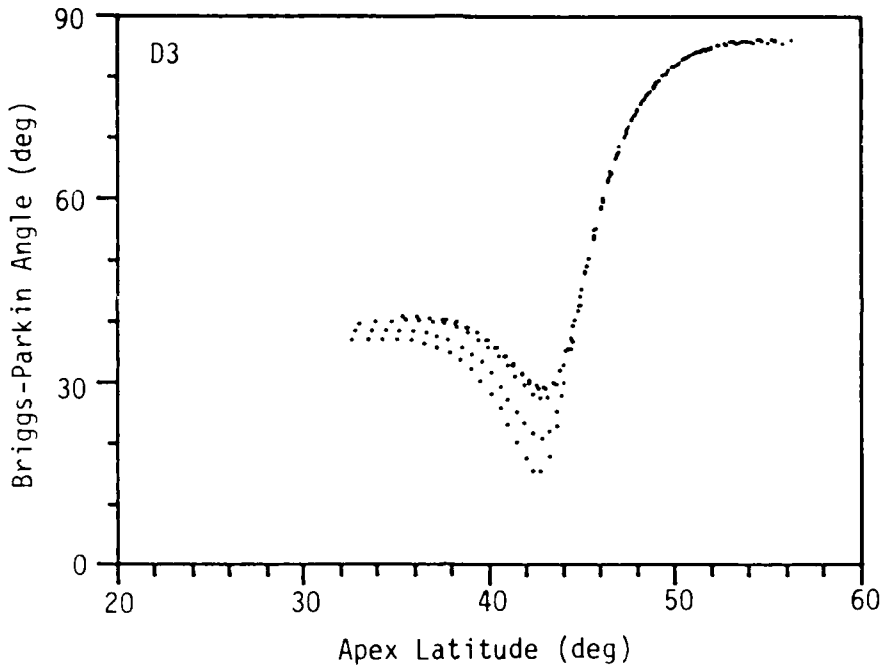

(c)

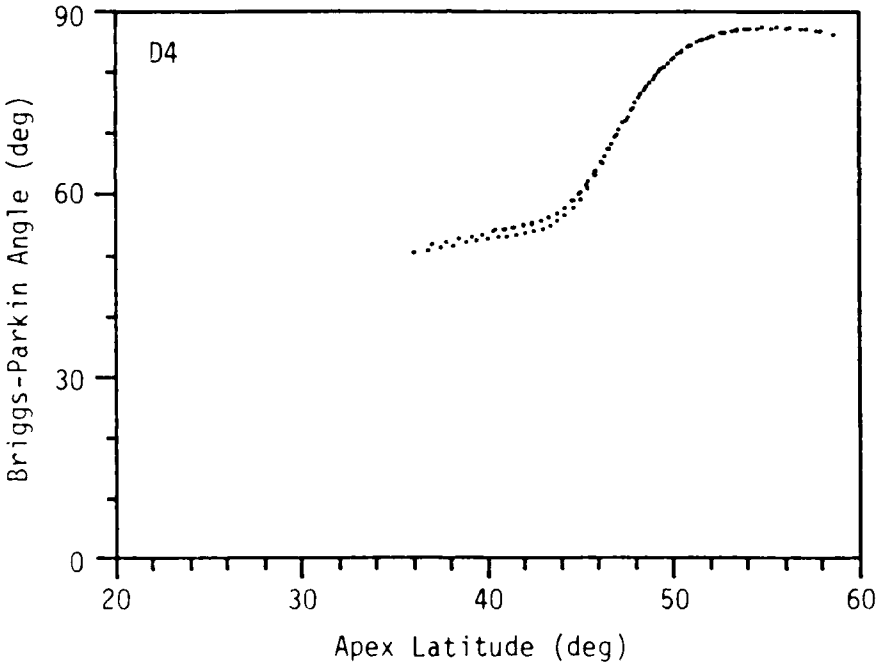

(d)

Figure 14. Scatter plots of Briggs-Parkin angle vs magnetic apex latitude, Λ_a, for daytime data corridors D1, D2, D3, D4, and D5. Plots are shown in (a), (b), (c), (d), and (e), respectively (Continued).

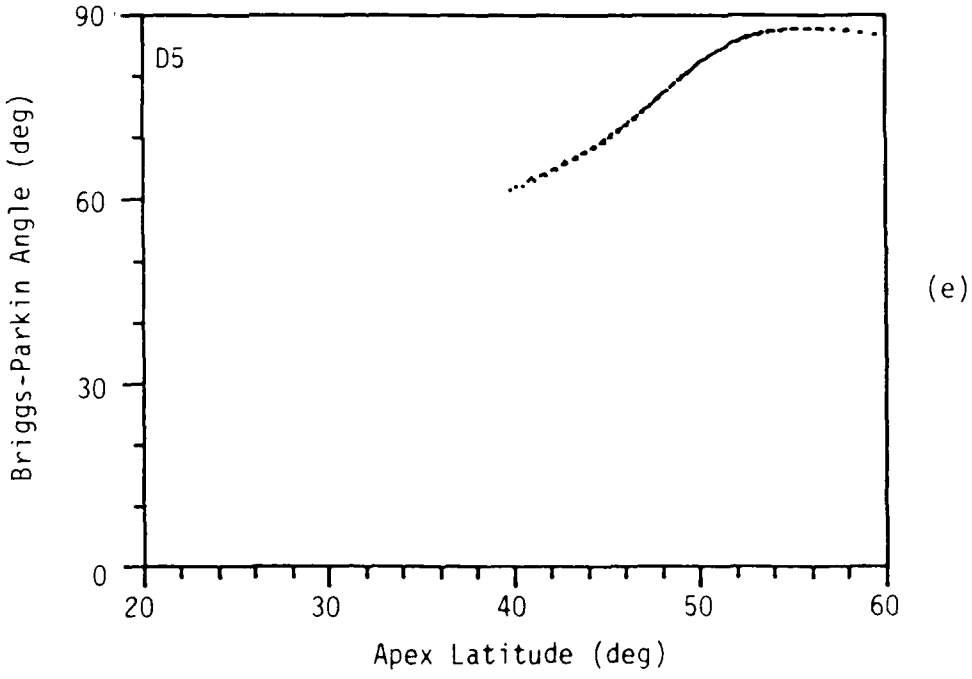

Figure 14. Scatter plots of Briggs-Parkin angle vs magnetic apex latitude, λ_a, for daytime data corridors D1, D2, D3, D4, and D5. Plots are shown in (a), (b), (c), (d), and (e), respectively (Concluded).

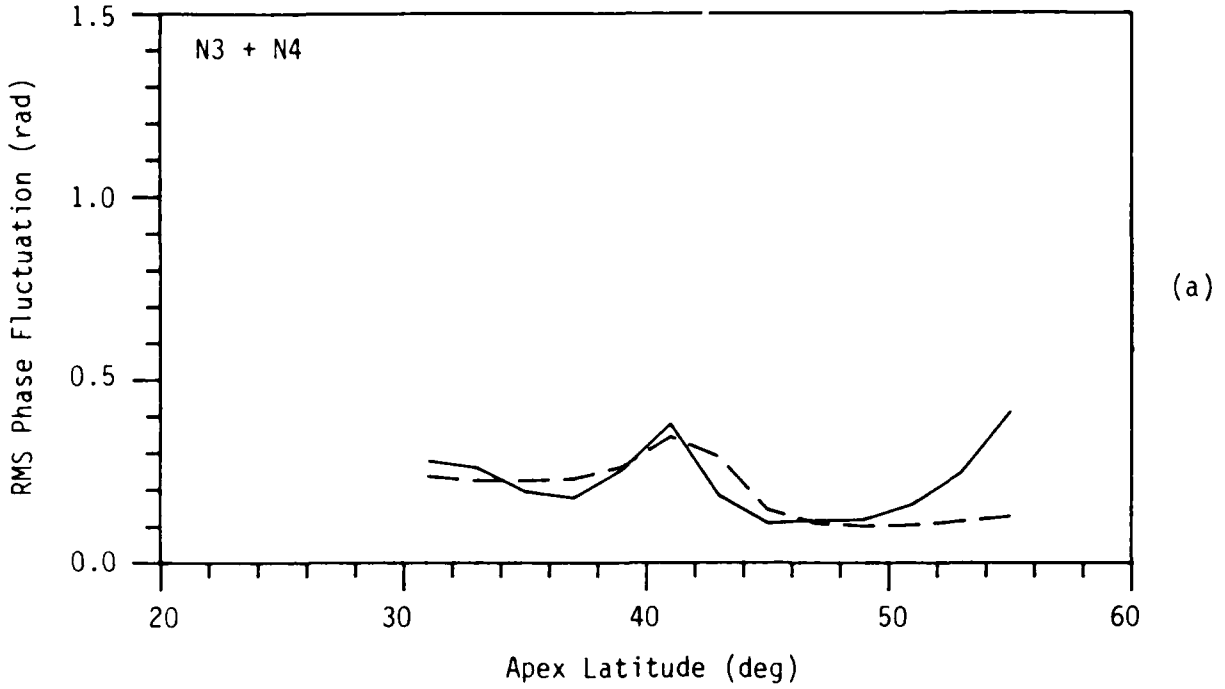

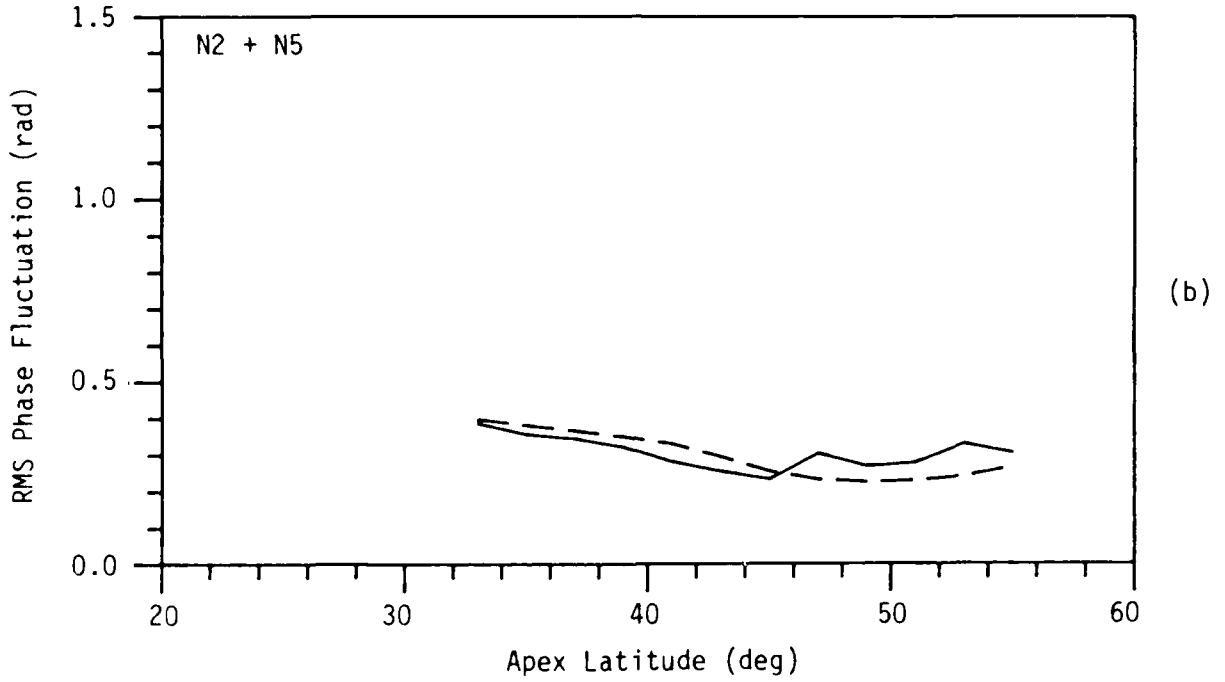

Figure 15. Bin-average plots of nighttime σ_ϕ *vs* λ_a for (a) the two most nearly overhead corridors (N3 and N4) and (b) two lower-elevation corridors (N2 and N5). Solid lines show results from observations, and dotted lines show results from WBMOD simulations. Latitude bins are 2° wide, and bins containing fewer than 30 points for (a) and 15 points for (b) are not shown.

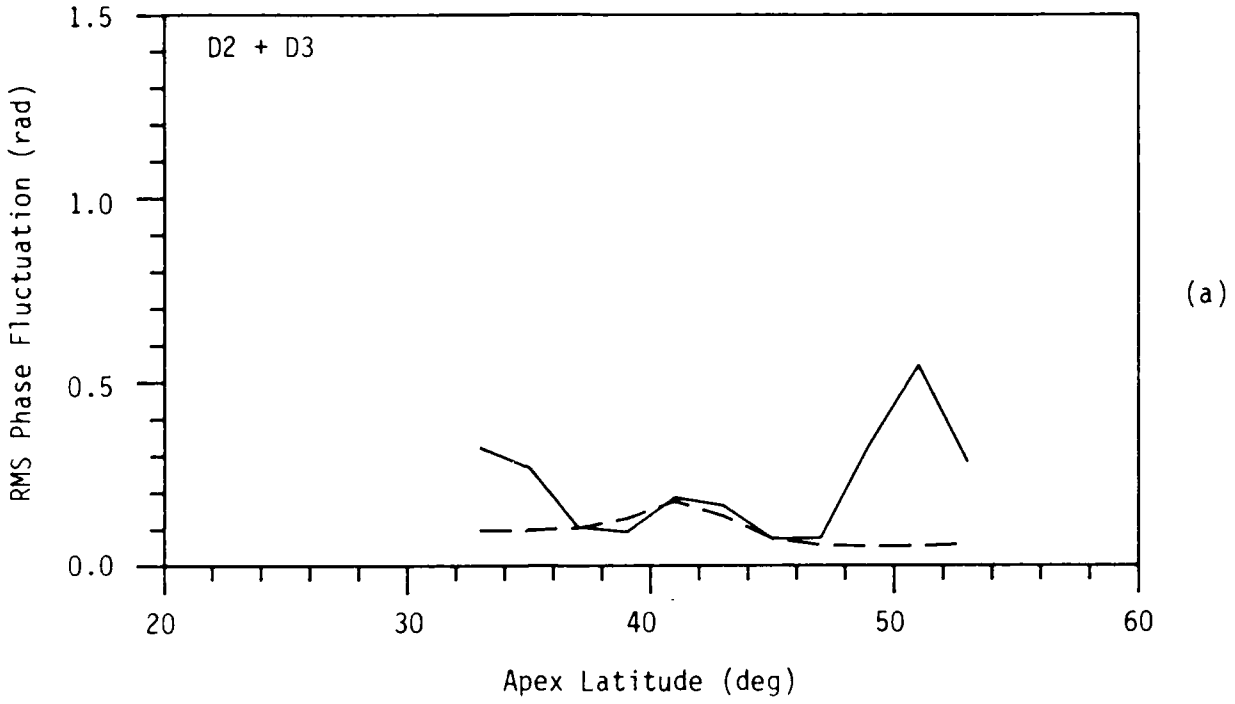

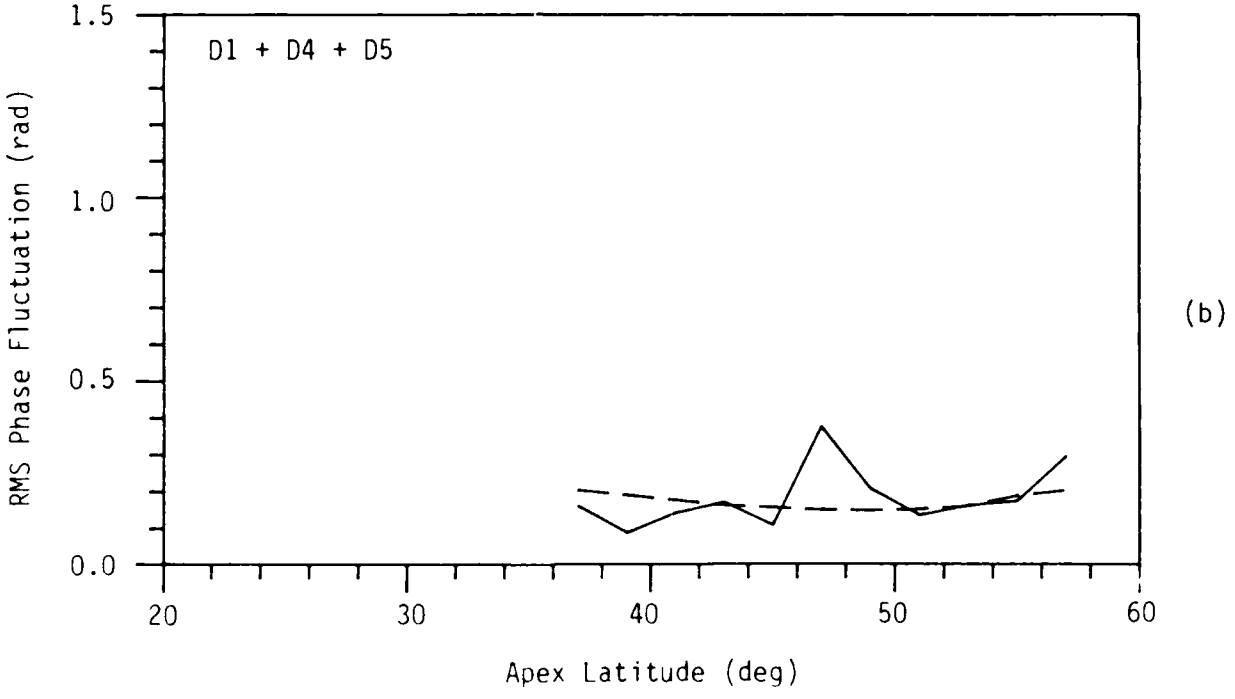

Figure 16. Bin-average plots of daytime σ_ϕ vs Λ_a for (a) the two most nearly overhead corridors (D2 and D3), and (b) three lower-elevation corridors (D1, D4 and D5). Solid lines show results from observations, and dotted lines show results from WBMOD simulations. Latitude bins are 2° wide, and bins containing fewer than 30 points for (a) and 15 points for (b) are not shown.

Bellevue HiLat data, we have determined a characterization of mid-latitude ambient F-layer radiowave scintillation and will include it in WBMOD, our global scintillation model. A general procedure presented in a previous report on the equatorial component of WBMOD has been used as a guide for mid-latitude model development.

As indicated in Table 2, our model describes the scintillation-producing irregularities as having cross-field isotropy, elongation along the magnetic field by a factor of 10, a single-regime power-law spectrum with an *in-situ* spectral index of 1.5, and representation by a phase-modulating screen located at an F-layer altitude of 350 km. In accord with an empirically based model of plasma drift, the irregularities are taken to drift eastward at night at speeds up to 20 m/sec and westward in the daytime at the same speeds.

The model describes the height-integrated spectral strength of the irregularities, $\log \overline{C_k L}$, by means of the following formulation:

$$\log \overline{C_k L} = C + f_T(t) + f_R(\bar{R}) \tag{7}$$

where t = local apex time (hours),

and $\bar{R}$ = smoothed Zurich sunspot number;

and where $f_T = 0.15 \cos \frac{2\pi t}{24}$, (8)

$$f_R(\bar{R}) = 0.002\ \bar{R}, \tag{9}$$

and $C_M = 14.50$.

We have introduced no apex-latitude dependence for mid-latitude $C_k L$ and have used error functions to merge the mid-latitude model with the equatorial and auroral models.

The mid-latitude model in WBMOD produces representative average scintillation levels for $35° \leq \lambda_a \leq 45°$ and successfully characterizes the effects of geometric enhancement for radiowave transmissions having Briggs-Parkin angles approaching zero. No attempt is made to model increasing scintillation trends observed in the Stanford data for $\lambda_a < 35°$ and $\lambda_a > 45°$. We await further observations from DNA's HiLat and Polar BEAR satellites to understand better scintillation activity occurring at apex latitudes falling between those represented by the auroral (Poker Flat) and the mid-latitude data. The transition between mid-latitude and equatorial (Ancon and Kwajalein) behavior remains to be explored.

SECTION 6

LIST OF REFERENCES

Fremouw, E.J. (1984), "Improvements in Operational Codes Describing the Ambient Ionosphere," Defense Nuclear Agency, Progress Report No. 9, Contract DNA001-83-C-0097, Physical Dynamics, Inc., Bellevue, WA.

Fremouw, E.J. and J.M. Lansinger (1981), "A Computer Model for High-Latitude Phase Scintillation Based on Wideband Satellite Data from Poker Flat," DNA Report 5686F, Contract DNA001-79-C-0372, Physical Dynamics, Inc., Bellevue, WA.

Fremouw, E.J. and R.E. Robins (1985), "An Equatorial Scintillation Model," Final Report for DNA Contract DNA001-83-C-0097, Physical Dynamics, Inc. Report No. PD-NW-85-342R, Bellevue, WA.

Fremouw and Secan, (1986), "Support of "Rover" Ground Station for DNA's HiLat Satellite," Progress Report for DNA Contract No. DNA001-85-C-0017, Physical Dynamics, Inc., Bellevue, WA.

Fremouw, E.J., R.L. Leadabrand, R.C. Livingston, M.D. Cousins, C.L. Rino, B.C. Fair, and R.A. Long (1978), "Early Results from the DNA Wideband Satellite Experiment - Complex-signal Scintillation," Rad. Sci., 13 (1), 167-187.

Fremouw, E.J., H.C. Carlson, T.A. Potemra, P.F. Bythrow, C.L. Rino, J.F. Vickrey, R.L. Livingston, R.E. Huffman, C.I. Meng, D.A. Hardy, F.J. Rich, R.A. Heelis, W.B. Hanson and L.A. Wittwer (1985), "The HiLat Satellite Mission," Rad. Sci., 20 (3), 416-424.

Livingston, R.C., C.L. Rino, J.P. McClure, and W.B. Hanson (1981), "Spectral Characteristics of Medium-Scale Equatorial F-Region Irregularities," J. Geophys. Res., 86 (4) 2421-2428.

Richmond, A.D., M. Blanc, B.A. Emery, R.H. Wand, B.G. Fejer, R.F. Woodman, S. Ganguly, P. Amayenc, R.A. Behnke, C. Calderon, and J.V. Evans (1980), "An Empirical Model of Quiet-Day Ionospheric Electric Fields at Middle and Low Latitudes," J. Geophys. Res., 85 (A9), 4658-4664.

Rino, C.L. (1979), "A Power Law Phase Screen Model for Ionospheric Scintillation. 1. Weak Scatter," Rad. Sci., 14 (6), 1135.

Rino, C.L., E.J. Fremouw, R.C. Livingston, M.D. Cousins, and B.C. Fair (1977), "Wideband Satellite Observations," DNA Report 4399F, Contract DNA001-75-C-0111, SRI International, Menlo Park, CA.

Secan, J.A. and E.J. Fremouw (1983a), "Improvement of the Scintillation-Irregularity Model in WBMOD," DNA Report TR-81-241, Contract DNA001-81-C-0092, Physical Dynamics, Inc., Bellevue, WA.

Secan, J.A. and E.F. Fremouw (1983b), "Improvements in Operational Codes Describing the Ambient Ionosphere," Defense Nuclear Agency, Progress Report No. 2, Contract DNA001-83-C-0097, Physical Dynamics, Inc., Bellevue, WA.

Sinno, K. and H. Minakoshi (1983), "Experimental Results on Satellite Scintillations Due to Field-Aligned Irregularities at Mid-Latitudes," J. Atmos. Terr. Phys., 45 (8/9), 563-567.

APPENDIX A

REPLACEMENT OF $C_s L$ WITH $C_k L$

In developing power-law scintillation theory, Rino (1979) chose to characterize irregularity and phase-scintillation strength in spectral terms, owing to the practical indeterminacy of the ionospheric outer scale. As a measure of irregularity strength, he defined the quantity

$$C_s = 8^{3/2} \langle N_e^2 \rangle k_o^{p-2} \Gamma\left(\frac{p+1}{2}\right) \Big/ \Gamma\left(\frac{p-2}{2}\right) \tag{11}$$

where $\langle \Delta N_e^2 \rangle$ = the electron-density variance
k_o = the outer-scale wavenumber
and p = the two-dimensional (phase) power-law index.

The precise physical meaning of C_s is a bit obscure, although it is mathematically well defined. An approximate physical definition is that it is "numerically equal to" the spatial power spectral density (PSD) at a wavenumber of unity (i.e., at a scale size of 1 m/rad). It is to be recognized that C_s does not have the usual three-dimensional spatial PSD units, but rather units of $(el)^2/m^{(4+p)}$. Of more practical significance, its defining wavenumber is far outside the scintillation-producing spectrum and probably outside any true power-law regime.

For reasons soon to be demonstrated, we define a new irregularity strength parameter, C_k, very closely related to C_s, explicitly as the three-dimensional PSD of electron density at a wavenumber k. That is, first we use Eqs. (5) and (6) of Rino (1979) to write the spectrum as

$$S_N(k) = 8\pi^{3/2} \frac{\Gamma\left(\frac{p+1}{2}\right)}{\Gamma\left(\frac{p-2}{2}\right)} \langle \Delta N_e^2 \rangle \frac{k_o^{(p-2)}}{(k_o^2 + k^2)^{(p+1)/2}} \tag{12}$$

where anisotropy has been taken up in the definition of the wavenumber, k, and then we define

$$C_k = 8\pi^{3/2} \frac{\Gamma\left(\frac{p+1}{2}\right)}{\Gamma\left(\frac{p-2}{2}\right)} \langle \Delta N_e^2 \rangle \frac{k_o^{(p-2)}}{(k_o^2 + k_k^2)^{(p+1)/2}} \tag{13}$$

so that $$C_k = C_s / (k_o^2 + k_k^2)^{(p+1)/2} \tag{14}$$

and has true PSD units of $(el/m^3)^2/(rad/m)^3 = el^2/m^3$. For $k_k >> k_o$, we have

$$C_k \approx 8\pi^{3/2} \frac{\Gamma\left(\frac{p+1}{2}\right)}{\Gamma\left(\frac{p-2}{2}\right)} \left\langle \Delta N_e^2 \right\rangle \frac{k_o^{(p-2)}}{k_k^{(p+1)}} = \frac{C_s}{k_k^{(p+1)}} \tag{15}$$

Next, we choose k_k to be $2\pi/10^3$ rad/m (i.e. a scale size of 1 km/cycle). We then have, to a good approximation,

$$C_k = 4\sqrt{\pi} \times 10^3 \left(\frac{10^3}{2\pi}\right)^p \frac{\Gamma\left(\frac{p+1}{2}\right)}{\Gamma\left(\frac{p-2}{2}\right)} \left\langle \Delta N_e^2 \right\rangle k_o^{(p-2)} \tag{16}$$

$$\text{or} \quad C_k = \left(\frac{10^3}{2\pi} \text{ meters}\right)^{(p+1)} C_s \ . \tag{17}$$

The simple rescaling represented by Eq. (17) accomplishes two things. First, it produces a strength parameter, C_k, which is a true PSD. More important, it characterizes the strength in a portion of the spectrum relevant to scintillation research (a scale size of 1 km rather than one on the order of a meter). Using C_s instead of C_k causes an irregularity-strength data base derived from phase-scintillation measurements to be unrealistically sensitive to variations in spectral index, p, whether those variations are ordered or random and whether they are real or arise from experimental or numerical inaccuracies. That sensitivity stems from the "long lever arm" that one effectively is employing in extrapolating a measurement made in the kilometer-scale range to a characterization defined in the meter-scale range. We shall see that converting phase-scintillation measurements to C_s introduces a misleading dependence of the irregularity strength parameter on p.

To complete a consistent procedure, we also define a new (in principle) parameter for characterizing the strength of phase scintillation, starting with that defined by Rino (1979) as

$$T = r_e^2 \lambda^2 \frac{\pi^{\frac{1}{2}} \Gamma(p/2)}{(2\pi)^{(p+1)} \Gamma\left(\frac{p+1}{2}\right)} (L \sec\theta) \, GC_s \, V_e^{(p-1)} \tag{18}$$

where r_e = classical electron radius,

λ = radio wavelength,

L = thickness of the irregular layer,

θ = incidence angle of the propagation vector on the layer,

and V_e = the effective (anisotropic) scan velocity.

Again T is approximately numerically equal to but not identical with a PSD, namely the temporal PSD of phase at a fluctuation frequency of 1 Hz. It has units of $rad^2/Hz^{(1-p)}$.

Analagous to C_k, we define T_1 explicitly as the PSD of phase (in rad^2/Hz) at fluctuation frequency ν_1, namely

$$T_1 = r_e^{2\nu^2} \frac{\pi^{\frac{1}{2}}\Gamma(p/2)}{(2\pi)^{(p+1)}\Gamma\left(\frac{p+1}{2}\right)} (L \sec\theta)\, GC_k \frac{(k_o^2 + k_k^2)^{(p+1)/2}}{(\nu_o^2 + \nu_1^2)^{p/2}} V_e^{(p-1)} \qquad (19)$$

where $\nu_o = V_e \frac{k_o}{2\pi}$.

From Eqs. (13), (18), and (19), we have, obviously,

$$T_1 = T/(\nu_o^2 + \nu_1^2)^{p/2} . \qquad (20)$$

Again in the large-outer-scale limit, we have

$$T_1 \approx r_e^{2\nu^2} \frac{\pi^{\frac{1}{2}}\Gamma(p/2)}{(2\pi)^{(p+1)}\Gamma\left(\frac{p+1}{2}\right)} \frac{k_1^{(p+1)}}{\nu_1^p} (L \sec\theta)\, C_k G\, V_e^{(p-1)} = \frac{T}{\nu_1^p} \qquad (21)$$

and, defining ν_1 at 1 Hz, we can obtain $C_k L$ to a good approximation from

$$C_k L = \frac{(10^3)^{(p+1)}\Gamma\left(\frac{p+1}{2}\right) T_1 \cos\theta}{\pi^{\frac{1}{2}}\Gamma\left(\frac{p}{2}\right) r_e^{2\nu^2} G V_e^{(p-1)}} \qquad (22)$$

where $T_1 = (1\ Hz)^p\ T$.

Experimentally, the parameter usually referred to as T really is T_1, the two being numerically equal (in the large-outer-scale limit). We shall make no further distinction between them. The distinction between C_s and C_k is of considerable practical importance, however, as we shall now see.

Repeatedly, it is reported that the spectral index, p (and its one-dimensional counterpart, q = p-1), decreases (portrays a shallower spectrum) as irregularity strength, characterized by C_s (or its height-integrated counterpart $C_s L$), increases. In dealing with the HiLat data from Rover, we again found this dependence, as illustrated in Figure 17a. The sample distribution of the contributing data population also is shown. The trend is very consistent for all $\log(C_s L)^{\frac{1}{2}}$ data bins having more than about 100 samples.

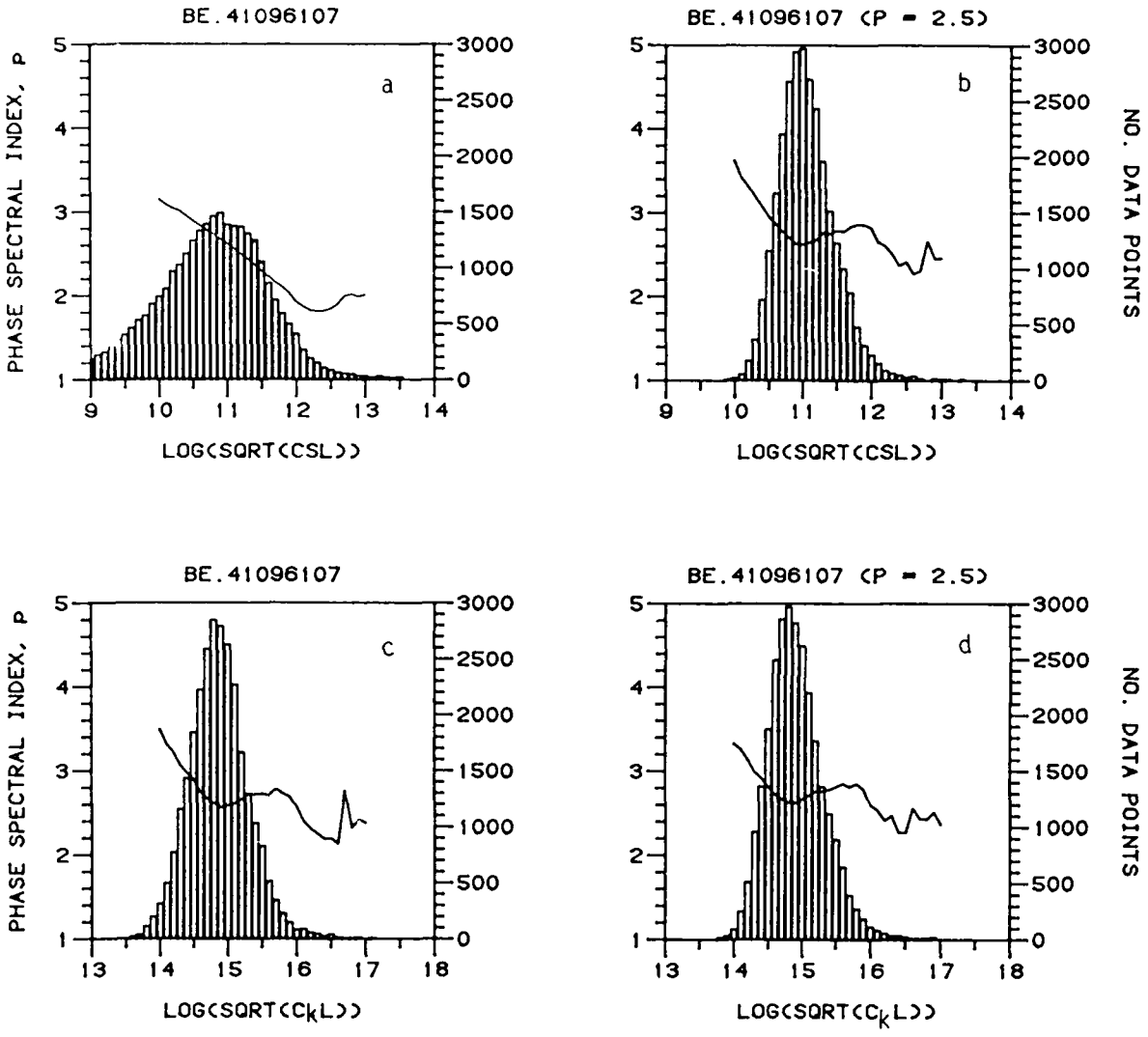

Figure 17. Relationship between bin averages of phase spectral index, p, measured with Rover at Bellevue and four measures of irregularity strength derived from spectral strength, T, of VHF phase scintillation. Also shown are occurrence distributions for the four strength measures. (a) C_sL computed from Eq.(18), employing measured values of p in the transformation. (b) C_sL computed from Eq.(18), employing a fixed value (2.5) of p in the transformation. (c) C_kL computed from Eq. (22), employing measured values of p. (d) C_kL computed from Eq. (22), employing a fixed value (2.5) of p. Note that only the first procedure results in a consistent trend between p and the strength parameter.

Indeed, our geophysical intuition suggests that the trend in Figure 17a is "too good to be true." Accordingly, we checked for the same trend in T, the observable from which the derived quantity $C_s L$ was obtained. The empirical relationship between p and $\sqrt{T \cos \theta}$ and the corresponding sample distribution are shown in Figure 18. A trend is evident only for bins with relatively few points, albeit still a goodly number.

Believing now that the consistent trend in Figure 17a was introduced in the conversion from T to $C_s L$, we checked for it in the empirical relationship between the measured p values and the latter quantity derived using a representative but fixed value of p (2.5) instead of the measured values. The result is shown in Figure 17b, from which the consistency of the trend in Figure 17a again is absent, reinforcing our disbelief in its underlying significance.

Next, we employed Eq. (22) to obtain $C_k L$, using the measured values of p for the conversion, and plotted its relationship with p in Figure 17c. Its similarity to Figure 17b makes us believe that it represents more nearly the true relationship between irregularity strength and spectral index in the Rover data population than the simple trend in Figure 17a. This belief is further reinforced by Figure 17d, which was obtained from Eq. (22) using a fixed value of p (2.5) for the conversion. That is, out of the four procedures represented in Figure 17, only the one employing the long lever arm of extrapolation imposed by solving Eq. (18) for C_s produces the clean trend often reported as the relationship between irregularity strength and spectral index.

We shall now demonstrate that employing the C_s "lever arm" introduces the reported clean trend into a data set having absolutely no underlying relationship between observed scintillation strength and spectral slope. To do so, we produced a simulated data population of p and T cos θ values, the sample distribution of the former being modeled after that actually observed in the Rover data population, and the distribution of the latter being uniform between 10^{-5} and 10^{-3} rad^2/Hz. Figure 19 shows the distribution of p values actually measured at VHF in Bellevue. For the simulation, we employed a gaussian fit to this distribution, having a mean value of 2.7 and a standard deviation of 0.71. We produced the simulated data set by applying the Gaussian p distribution repeatedly to points within each of the equally populated T bins. Thus, there was no correlation between p and T.

We then used Eq. (18) to compute $C_s L$ from the simulated data base, employing fixed values of 1.0 for G and 1500 m/sec for V_e. The relationship between the input p values and the output $C_s L$ values is indicated by the solid curve in Figure 20a. It is represented very well by a straight line with a slope of -0.59, as obtained from a best

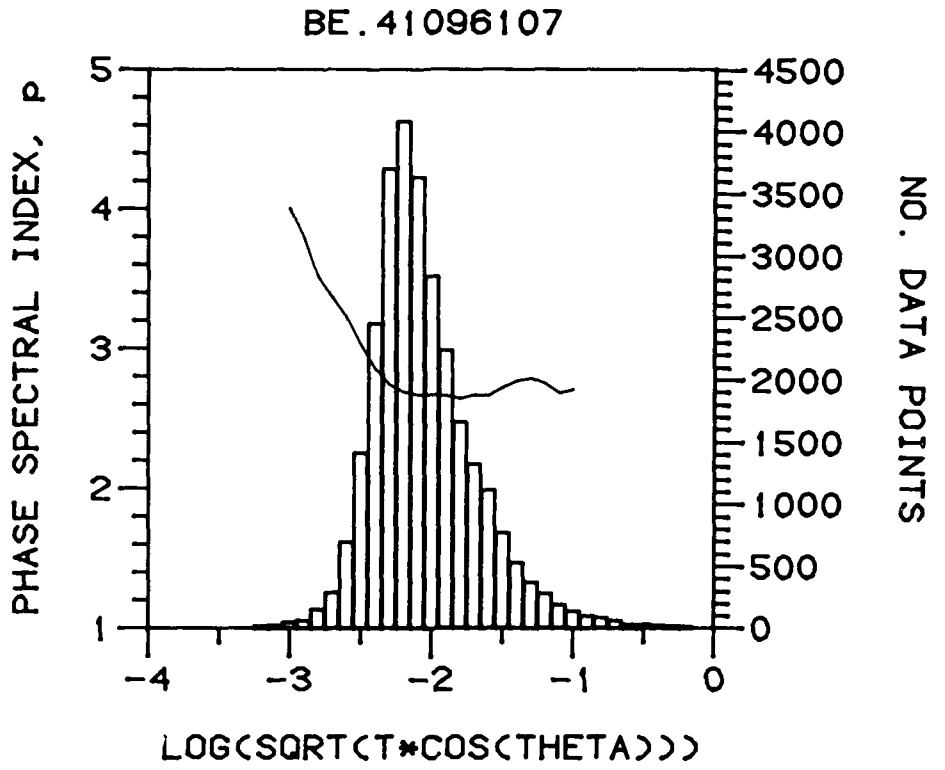

Figure 18. Relationship between bin averages of phase spectral index, p, and spectral strength, T, of VHF phase scintillation directly measured at Bellevue. Occurrence distribution of T also is shown.

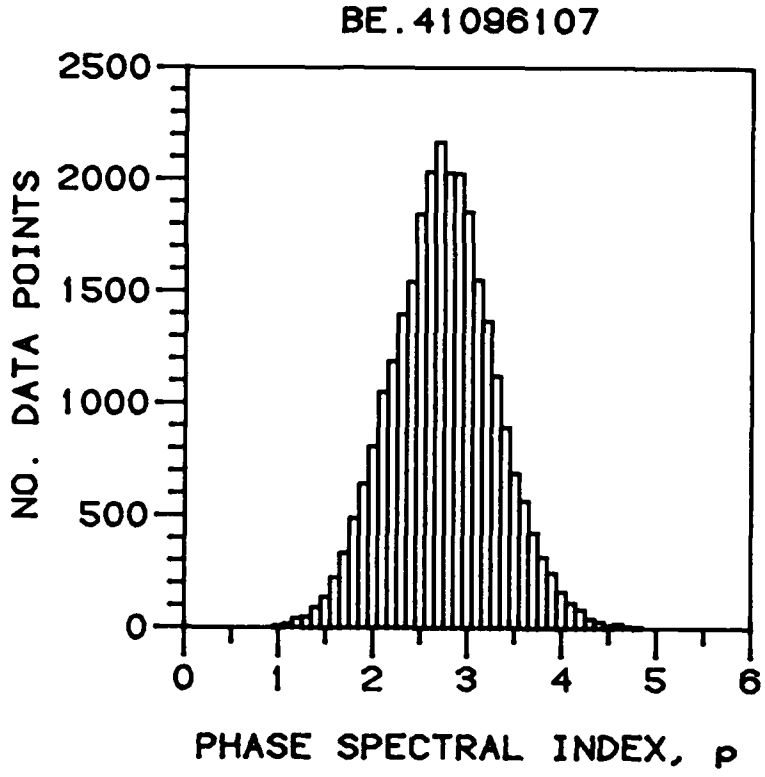

Figure 19. Occurrence distribution of VHF phase spectral index measured at Bellevue between Day 109 of 1984 and Day 107 of 1986 (same population as in all other figures containing observed data).

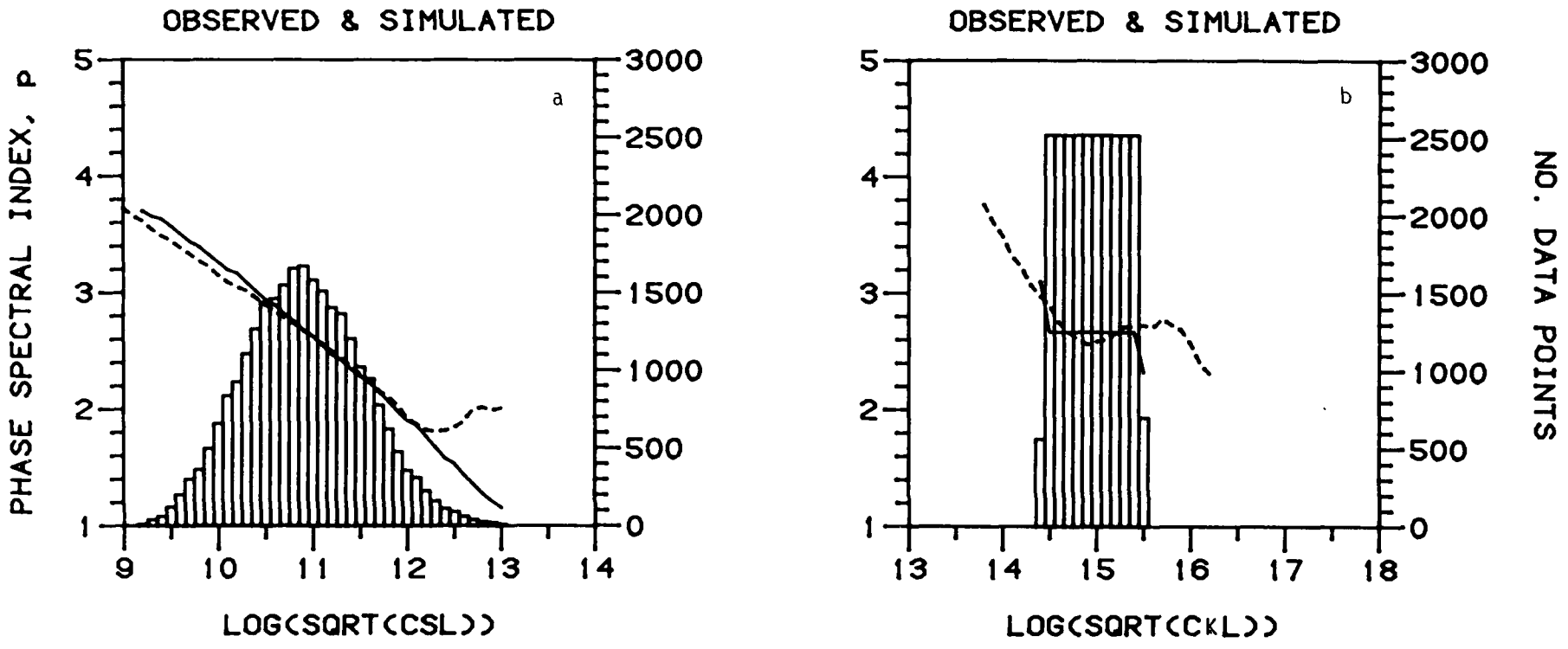

Figure 20. Relationships between phase spectral index, p, and two measures of irregularity strength for observed (broken) and simulated (solid) data sets. (a) C_sL computed from Eq. (18). (b) C_kL computed from Eq. (22). In both cases, the simulated data sets contained absolutely no correlation between p and the parameter, T, from which the strength measure was computed. The distribution of T was uniform (and truncated). Transformation to C_sL has altered the distribution to resemble that of p (which was a Gaussian fit to Figure 19), while transformation to C_kL has preserved the uniform distribution except at the truncation edges.

fit over the range $10 \leq \log (C_s L)^{\frac{1}{2}} \leq 12$. This is essentially identical to the relationship between p and log ($C_s L$) with a slope of -0.3 reported by Livingston *et al* (1981) and with the trend displayed in Figure 17a, which is repeated as the broken curve in Figure 20a. The histogram in Figure 20a illustrates the distribution of $C_s L$ values resulting from application of Eq. (18) to a uniformly distributed (albeit truncated) population of T values, given a p distribution such as the observed one illustrated in Figure 19.

Finally, we converted our simulation data base from T to $C_k L$, using Eq. (22). Those results are displayed in Figure 20b along with the corresponding relationship between p and $C_k L$ from the observed data base. The uniform distribution of input T values from the simulated data population has survived transformation to $C_k L$, except near its truncation edges, as indicated by the histogram. A few T values near the edges have been converted preferentially to the smallest (largest) $C_k L$ values by large (small) p values, as indicated by the solid curve. The relationship between measured p and $C_k L$ derived from the measured T values displays a somewhat similar behavior, as indicated by the broken curve.

We conclude from the foregoing that the relationship between irregularity strength and spectral index often reported from measurements of phase scintillation is, at least, strongly amplified by the "lever arm" of extrapolation from measurements in the km-scale regime to characterization, by means of C_s from Eq. (18), in the meter-scale regime. We have, therefore, abandoned use of $C_s L$ in characterizing irregularity strength in favor of $C_k L$, obtained from the simple scaling indicated by Eq. (17).

APPENDIX B

PARTIAL RESOLUTION OF STANFORD/BELLEVUE DISCREPANCY

The first step in combining the results from the Stanford Wideband data set and the Bellevue (Rover) HiLat data set was to plot the apex latitude variation of log $\overline{C_k L}$ from the two data sets (Figure 21(a) shows scatter plots and Figure 21(b) shows bin-average plots.) As can be seen, there is a discrepancy of over half an order of magnitude between the $\overline{C_k L}$ values at the northern end of the Stanford data set and the southern end of the Bellevue data set. Two possible sources of this discrepancy were investigated:

1. Errors in the code developed to convert raw phase data to $C_k L$.
2. Differences in the methods used to calculate $C_k L$ from phase (σ_ϕ for the Stanford data set and the spectral parameters T and p for the Bellevue data set).

Regarding number 1, the implementations of the theory used in the conversion were checked carefully, and hand calculations for a selected number of points were compared to calculations from the software. No errors or problems were found in this area.

Regarding number 2, the equation for $C_k L$ as a function of the phase spectral parameters T and p developed in Appendix A (Equation (22)) was used to calculate $C_k L$ from the Bellevue/HiLat data base. This approach could not be used directly for the Stanford/Wideband data base, as the T and p parameters were not generated for this data set. However, the RMS phase parameter, σ_ϕ, can be converted to an equivalent T value. This equivalence follows from the assumption that the phase spectral density function (SDF) can be modeled in terms of the two parameters T (spectral power at 1 Hz) and p (spectral slope) as

$$SDF = Tf^{-p}. \tag{23}$$

Since the phase variance, σ_ϕ^2, is the integral of this function over all frequencies such that $f \geq f_c$, where f_c is the low-frequency cutoff (set in the Stanford data by the 0.1 Hz detrender cutoff), we get

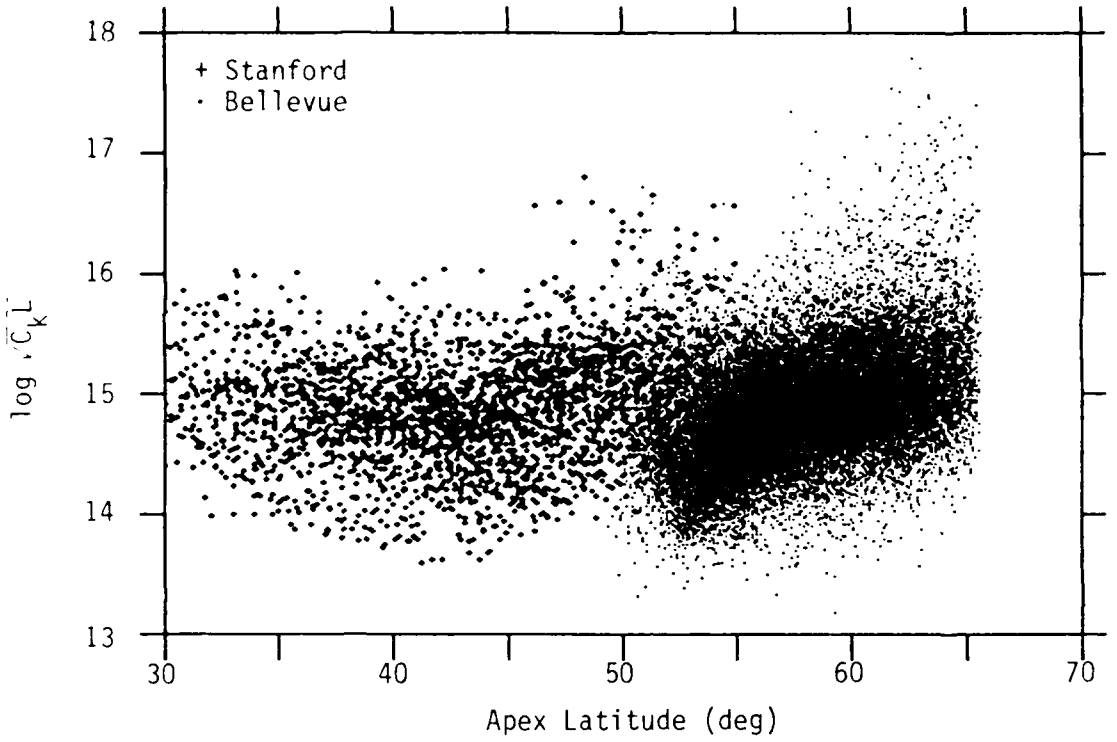

(a)

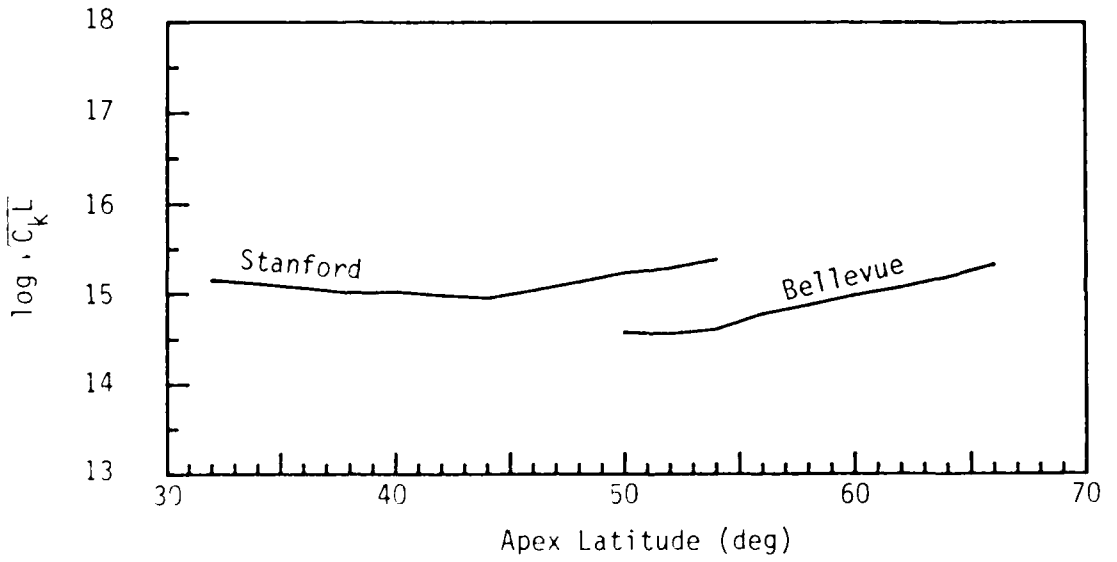

(b)

Figure 21. Variation of log $\sqrt{C_k L}$ with apex latitude from the Stanford Wideband and Bellevue HiLat data bases. (a) shows a scatter plot, where crosses denote Stanford data and dots denote Bellevue data; (b) shows bin average plots for each data set.

$$\sigma_\phi^2 = \frac{2T}{(p-1)} f_c^{-(p-1)} \tag{24}$$

or

$$T = 0.5(p-1) f_c^{(p-1)} \sigma_\phi^2 \, . \tag{25}$$

The major uncertainty in Equation (25) is the value to use for p. For the calculations used in creating Figure 21, a value of 2.5 was used; this choice was based on analysis of other Wideband data sets (Fremouw and Lansinger, 1981; Fremouw and Robins, 1985). The value of T calculated from Equation (25) and the assumed value of p can then be used to calculate $C_k L$.

In order to test this calculation, five Stanford/Wideband passes (listed in Table 4) were reprocessed to provide values for T and p as well as σ_ϕ. Figure 22 is a scatter plot of the T values calculated from the σ_ϕ values using Equation (25) with p = 2.5, plotted against the corresponding T values obtained from a log-linear fit to the actual phase SDF. The straight line is a linear least-squares fit to the data constrained to have a slope of 1.0.

Initially, the offset found from Figure 22 was to be used as an empirical correction to the Stanford T values, but a more detailed study of discrepancies between the spectral results from the Wideband data sets and those from the HiLat data sets (Fremouw and Secan, 1986) found that the p values from the Wideband data sets are artificially low. The Stanford passes were reprocessed using the standard HiLat processing, which yielded an average value for p of 2.85, which agrees well with the average p found in the low-latitude end of the Bellevue/HiLat data set.

Figure 23 is a scatter plot of the data in Figure 22, this time using p = 2.85 in calculating T from σ_ϕ. The offset is much smaller now, with a residual multiplicative correction of 0.8 to convert T calculated from σ_ϕ to the corresponding T extracted from the phase SDF. (Note: This residual probably is tied to the consistent steepening of the phase SDF reported in several recent reviews of both Wideband and HiLat data. As this tie is still under investigation, we have not attemped to resolve the issue here but have simply carried forward the correction factor).

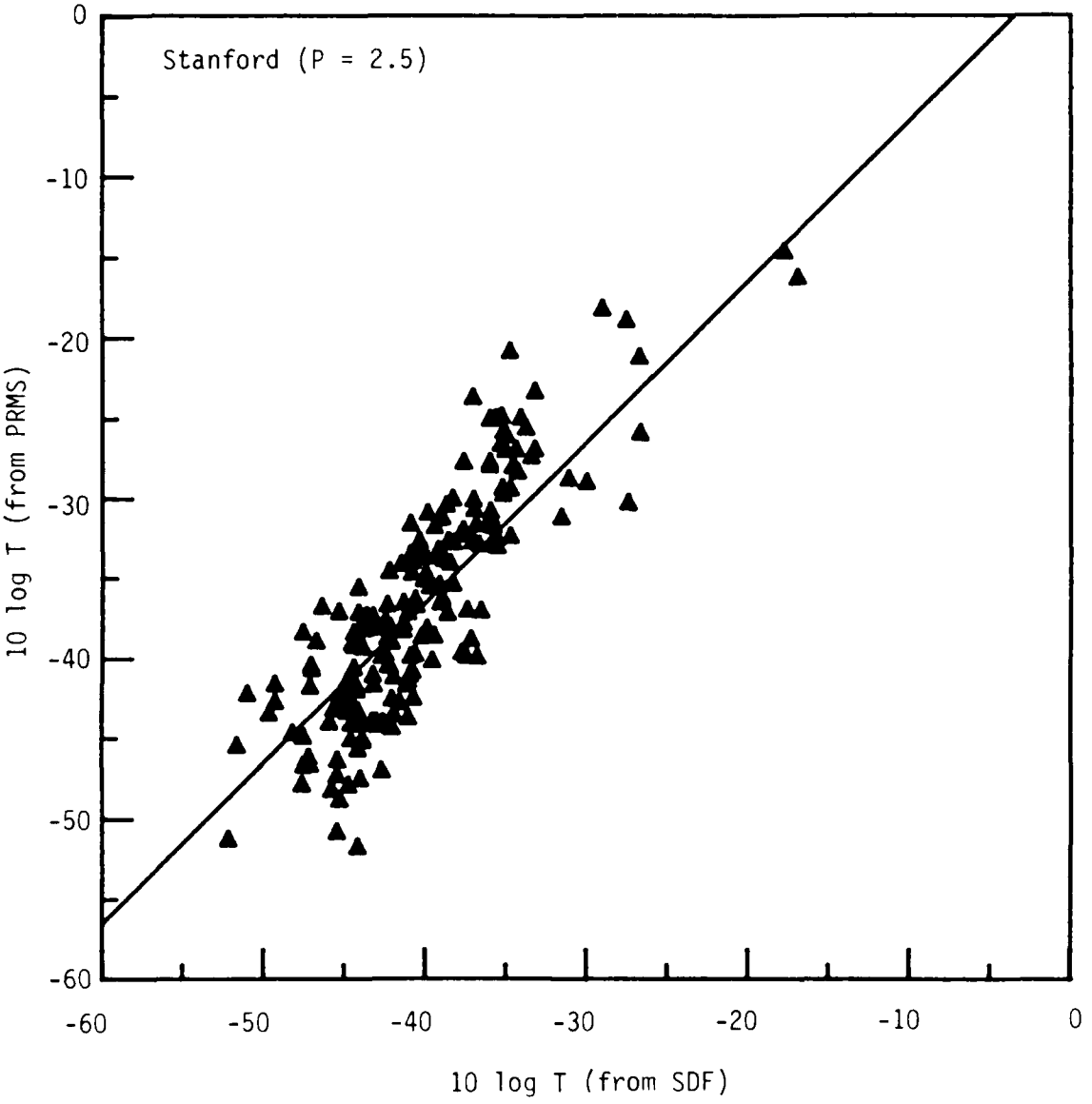

Figure 22. Comparison of the values 10 log T calculated from σ_ϕ (p = 2.5) to the values 10 log T extracted from the phase SDF, computed for five representative Stanford Wideband passes. The straight line is a least-squares fit to the data, constrained to have a slope of unity.

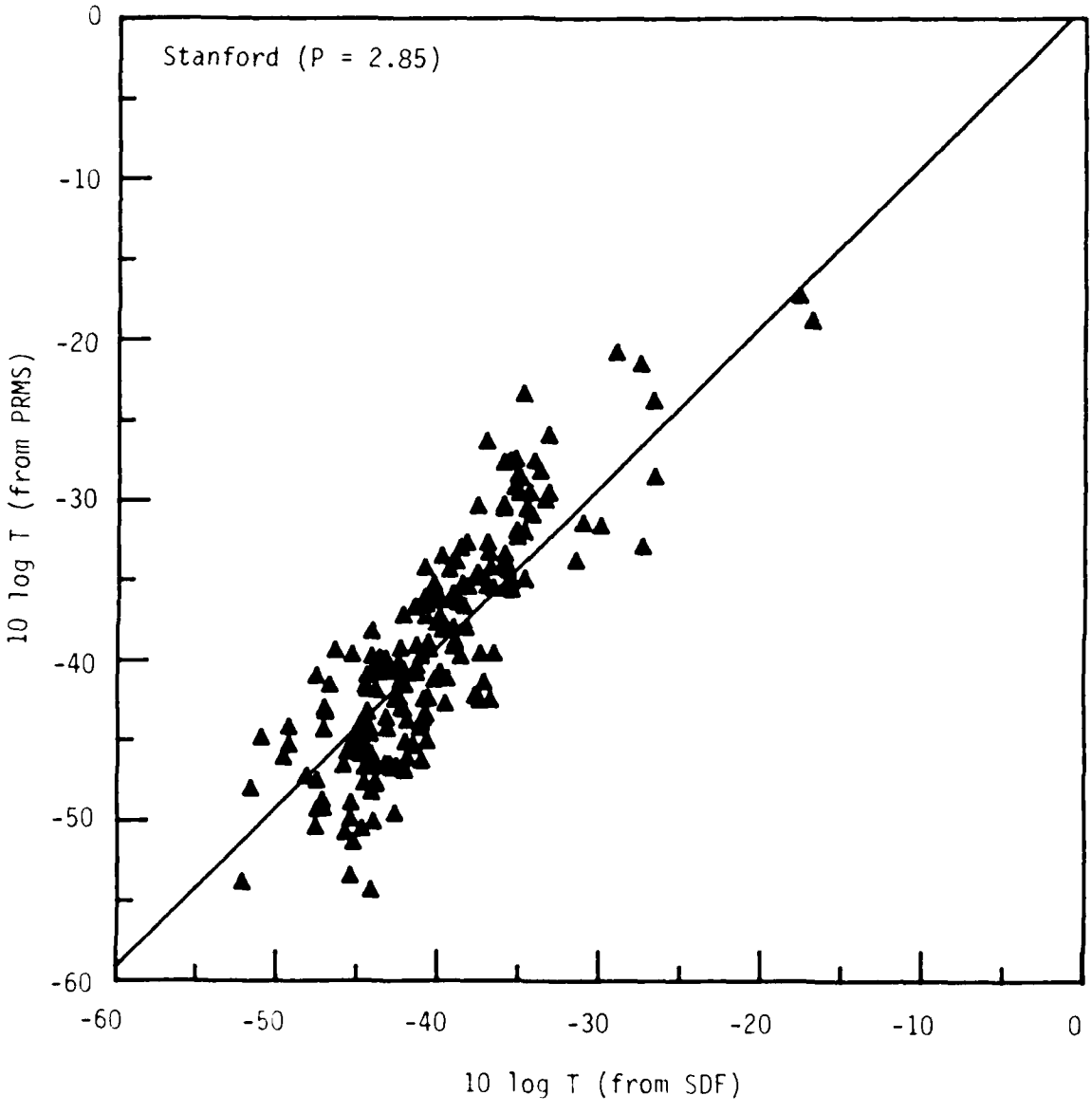

Figure [illegible]. Comparison of the values 10 log T calculated from [illegible] (p = 2.85) to the values 10 log T extracted from the phase SDF computed for five representative Stanford Wideband passes. This figure differs from Figure [illegible] only in the value of p used to calculate T from [illegible].

Table 4. Stanford/Wideband Passes Reprocessed.

Pass ID	Date	GMT
ST-01-41	1 Jul 76	17:31
ST-01-49	8 Jul 76	18:39
ST-02-25	6 Aug 76	06:55
ST-02-47	27 Aug 76	08:41
ST-10-04	4 Sep 76	07:00

Figure 24 is a repeat of the bin-averages in Figure 21(b) with an additional curve showing the new $\sqrt{C_k L}$ latitudinal variation for Stanford using a p value of 2.85 and the correction factor of 0.8. Although the Stanford and Bellevue curves are now closer together, they still differ by a factor of ~3. To explain this discrepancy, we hypohesized that the increase in $C_k L$ with latitude at the high-latitude end of the Stanford data set was due to urban radio noise from the San Francisco/Oakland area north of Stanford interfering with the VHF signal. To investigate this, both VHF and UHF_c (the center UHF channel) for the five Stanford passes listed in Table 4 were reprocessed, and the σ_ϕ values for the two frequencies were compared. Any noise contamination in only the VHF channel would cause a departure from the f^{-1} scaling expected in the observed σ_ϕ values.

Figures 25(a)-(c) and 26(a)-(c) show the results of the foregoing analysis for passes ST-01-49 and ST-02-25. The upper two plots in Figures 25(a) and 26(a) are the log intensity and detrended (at 0.1 Hz) phase for the VHF channel, and the bottom two plots are the log intensity and detrended phase for the UHF_c channel. Note that the ordinate scales on the VHF and UHF_c detrended phase plots reflect the theoretical f^{-1} scaling, which in this case is a factor of 3 between the Wideband VHF and UHF_c channels.

Figures 25(b) and 26(b) are scatter plots of σ_ϕ from UHF_c against σ_ϕ from VHF, and Figures 25(c) and 26(c) show the variation of log σ_ϕ for both VHF and UHF_c through the pass. Note that the axis scales on the scatter plots in Figures 25(b) and 26(b) have been set so that all points following the f^{-1} scaling fall along the diagonal from the lower left to upper right of the plot.

These foregoing figures, which are representative of the five passes reprocessed, show little evidence of a systematic noise contamination in the VHF data.

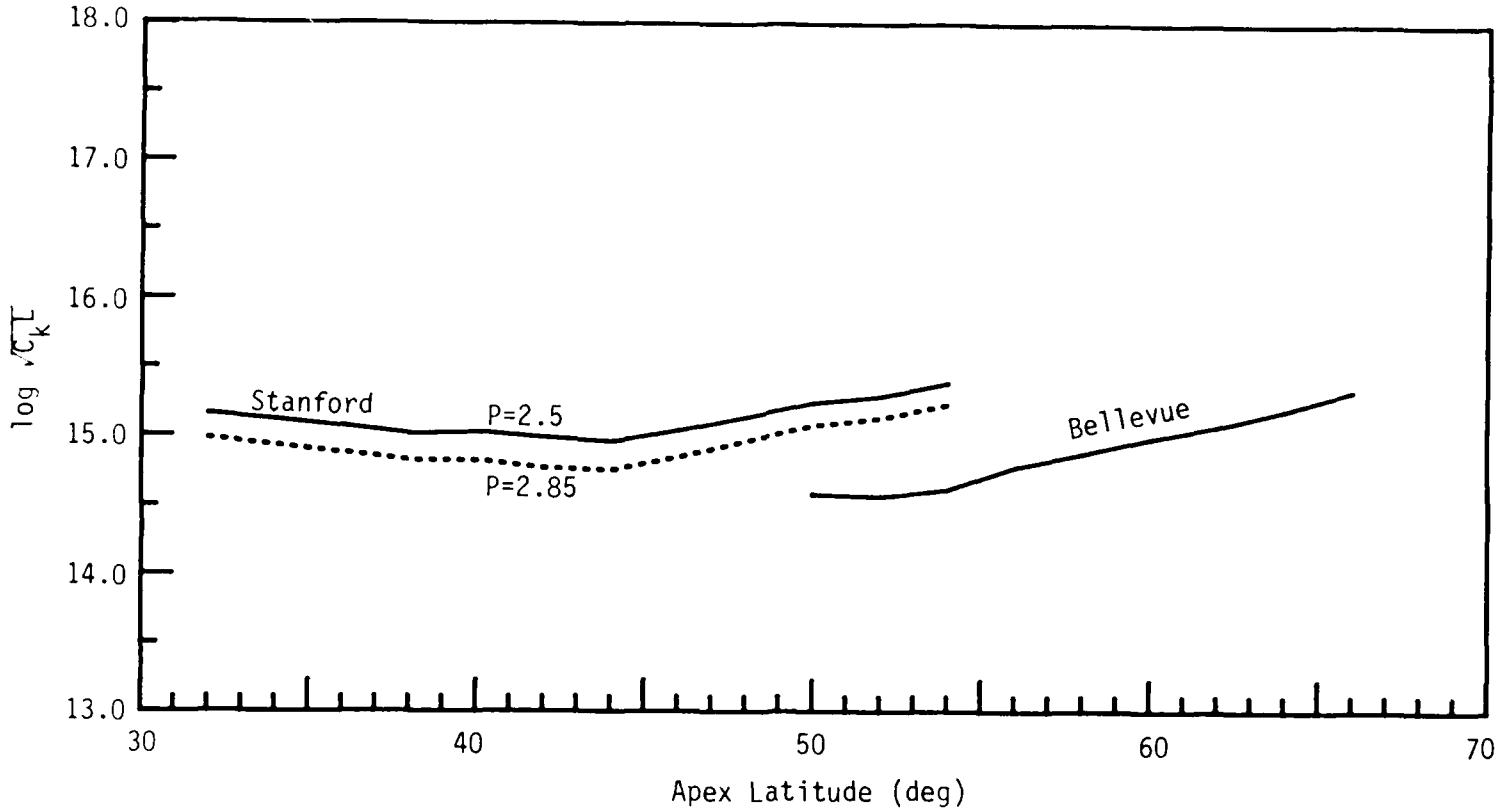

Figure 24. Bin-average plots of log $\sqrt{C_k L}$ *vs.* apex latitude for the Stanford Wideband and the Bellevue HiLat data bases. Solid lines are identical to the solid lines in Figure 21b. Dotted line shows the effect of calculating log $\sqrt{C_k L}$ for the Stanford data using p = 2.85 and a 0.8 adjustment factor.

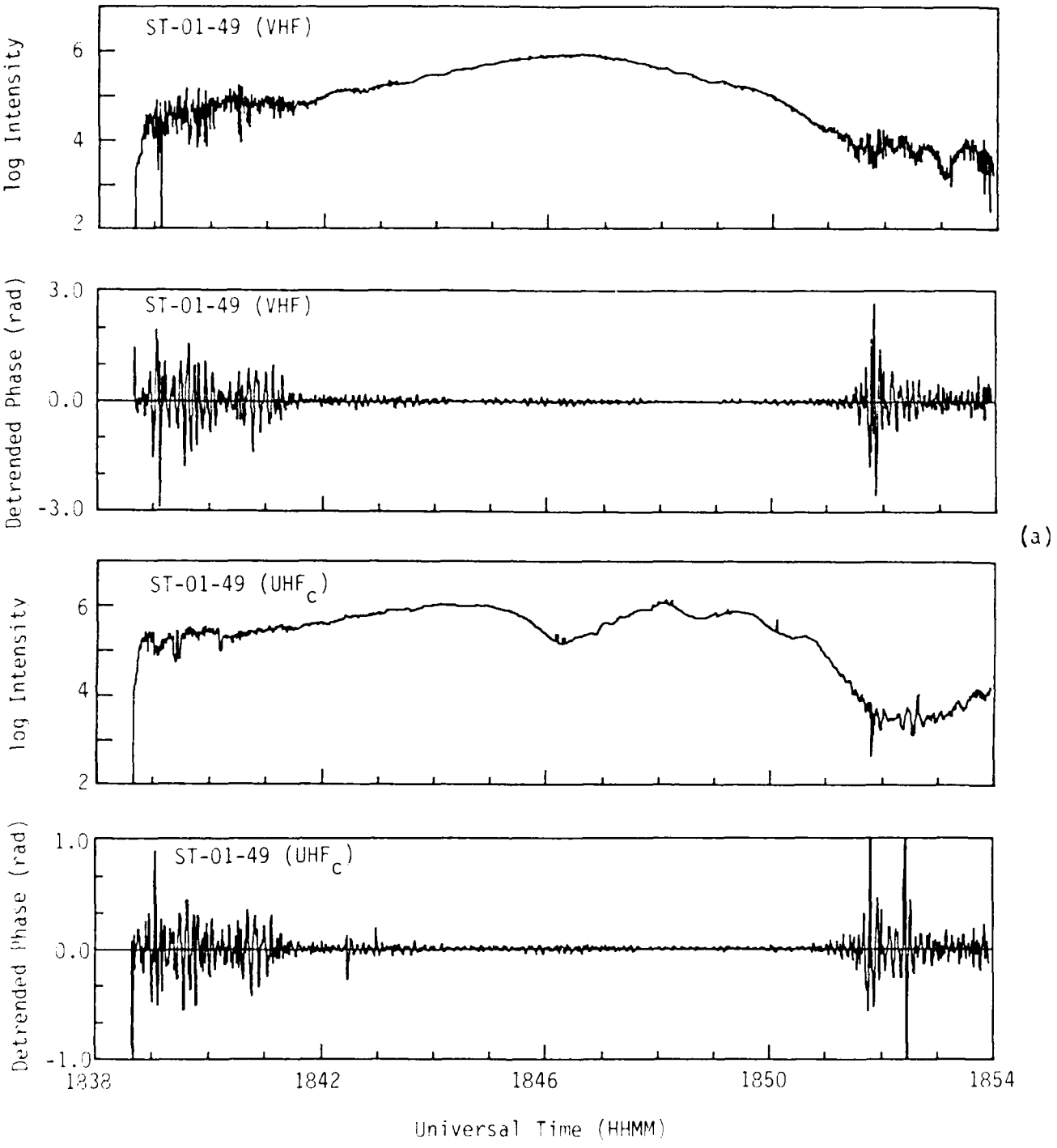

Figure 3. (a) VHF (upper plots) and UHF$_c$ (lower plots) channels for Wideband pass ST-01-49. Top plot in each pair is log intensity, bottom plot is phase detrended at 0.1 Hz. (b) Scatter plot of [illegible] at UHF$_c$ against [illegible] at VHF for Wideband pass ST-01-49. (c) Plot of VHF (upper) and UHF$_c$ (lower) log [illegible] time for Wideband pass ST-01-49.

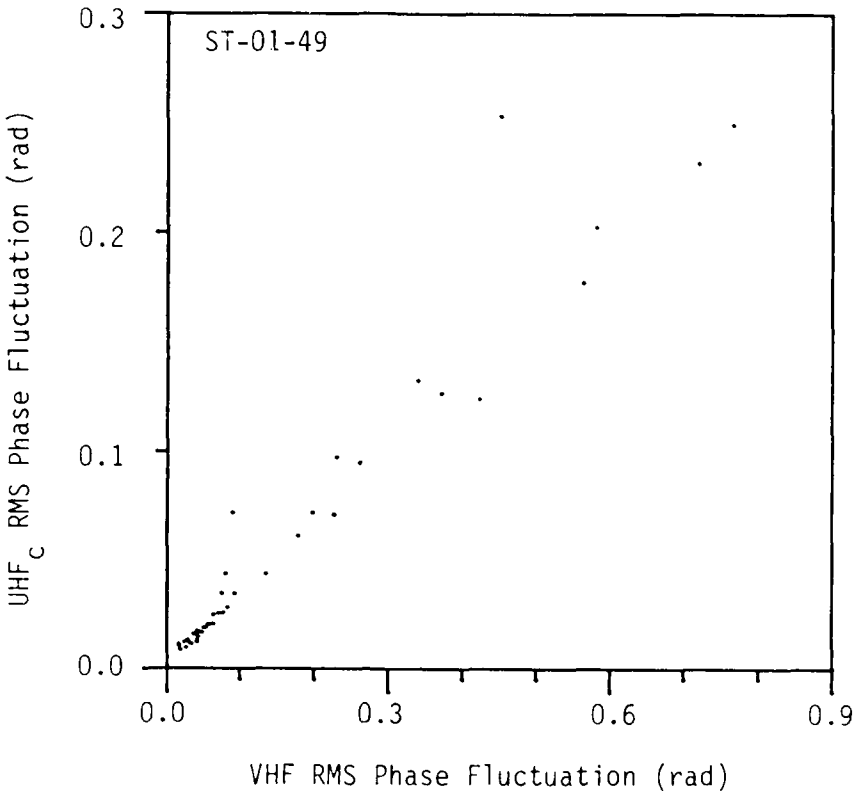

(b)

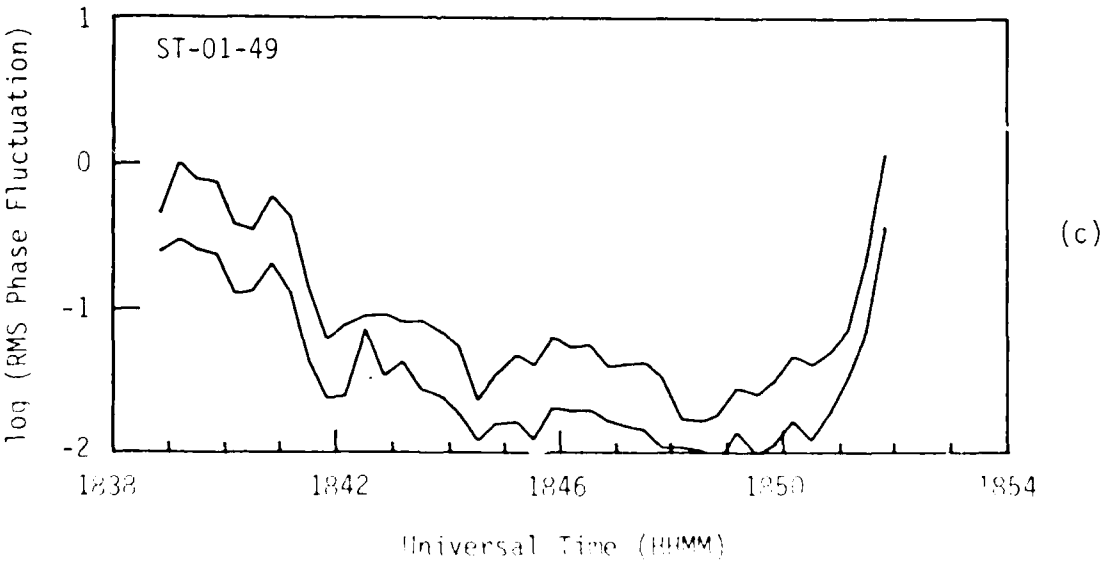

(c)

Figure 25. (a)VHF (upper plots) and UHF$_c$ (lower plots) channels for Wideband pass ST-01-49. Top plot in each pair is log intensity, bottom plot is phase detrended at 0.1 Hz. (b) Scatter plot of [illegible] at UHF$_c$ against [illegible] at VHF for Wideband pass ST-01-49. (c) Plot of VHF (upper) and UHF$_c$ (lower) log [illegible] vs time for Wideband pass ST-01-49 (no units).

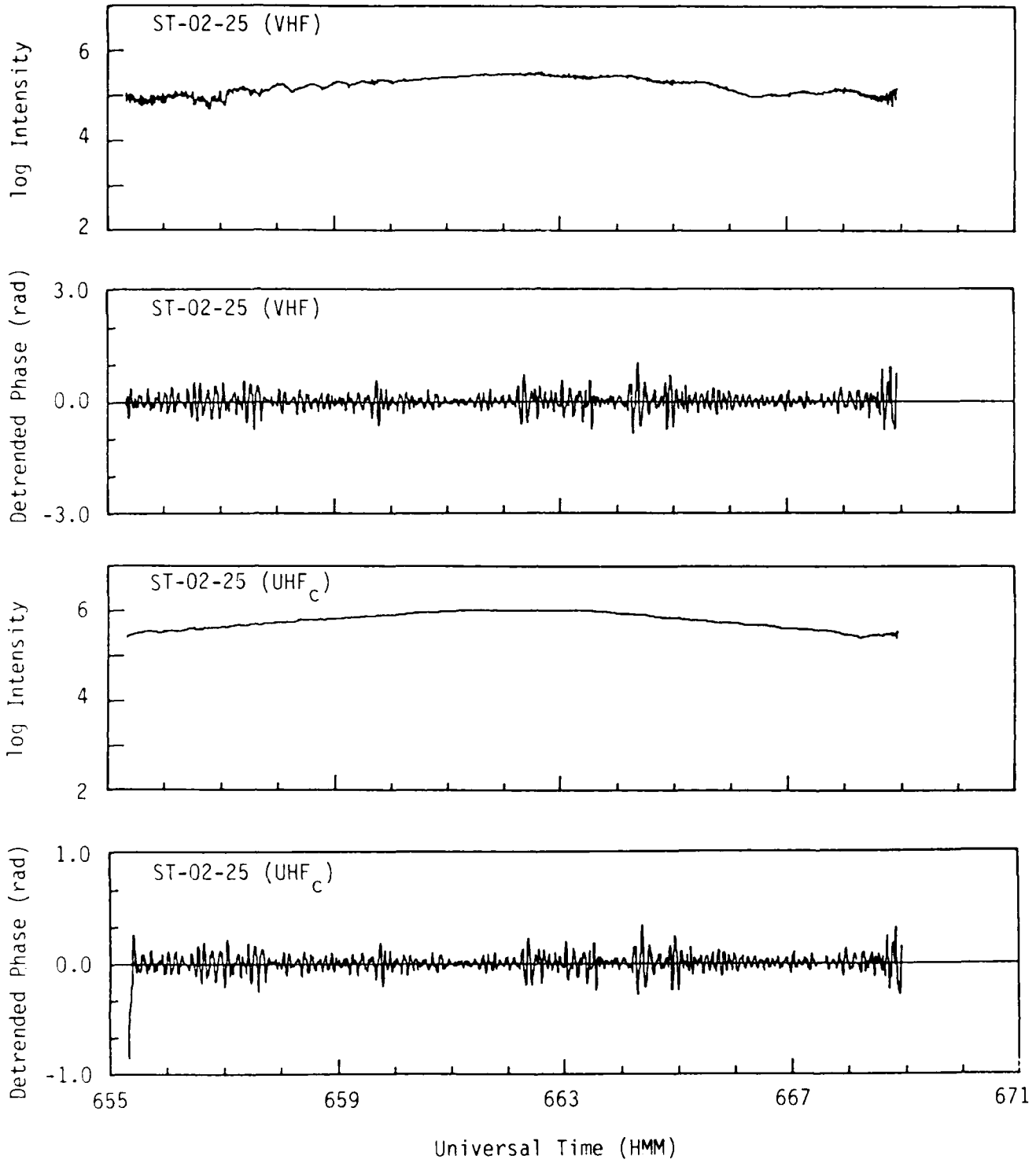

Figure 26. (a) VHF (upper plots) and UHF$_C$ (lower plots) channels for Wideband pass ST-02-25. Top plot in each pair is log intensity, bottom plot is phase detrended at 0.1 Hz. (b) Scatter plot of σ_ϕ at UHF$_C$ against σ_ϕ at VHF for Wideband pass ST-02-25. (c) Plot of VHF (upper) and UHF$_C$ (lower) log σ_ϕ vs time for Wideband pass ST-02-25.

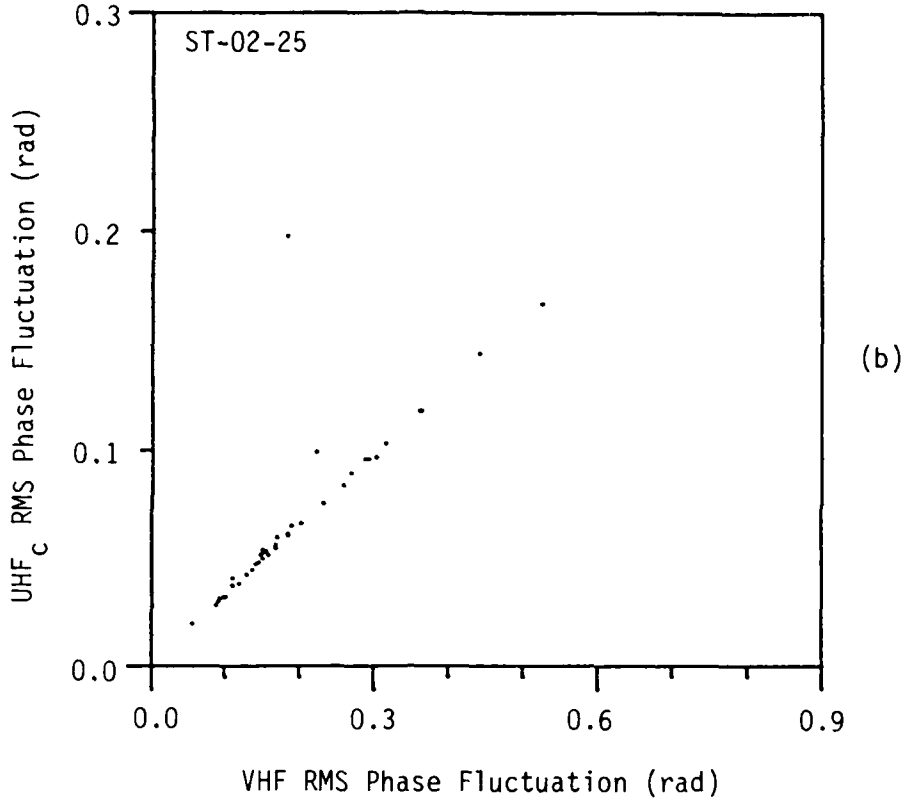

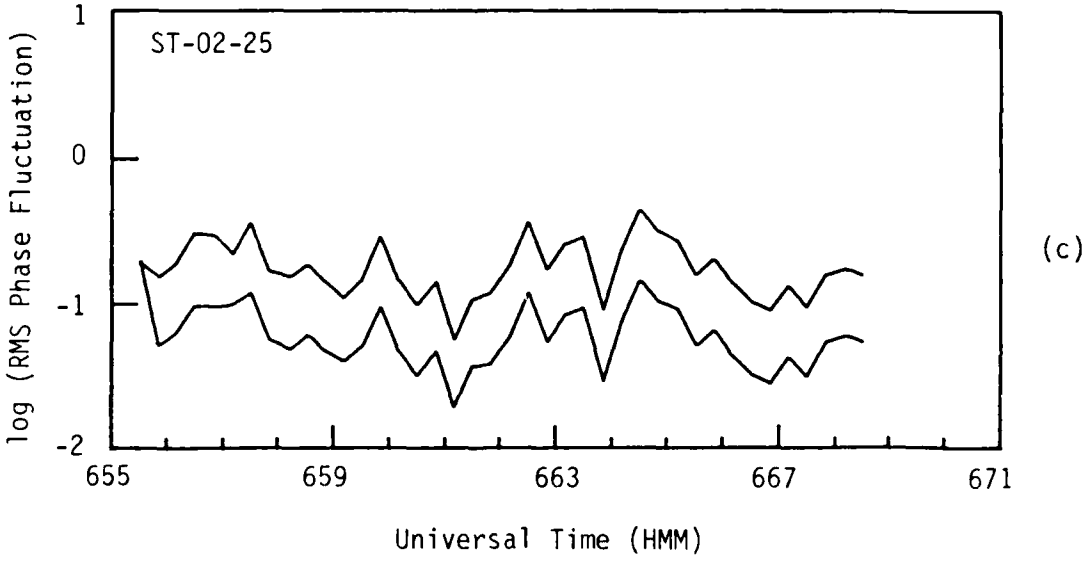

Figure 26. (a) VHF (upper plots) and UHF$_c$ (lower plots) channels for Wideband pass ST-02-25. Top plot in each pair is log intensity, bottom plot is phase detrended at 0.1 Hz. (b) Scatter plot of σ_ϕ at UHF$_c$ against σ_ϕ at VHF for Wideband pass ST-02-25. (c) Plot of VHF (upper) and UHF$_c$ (lower) log σ_ϕ vs time for Wideband pass ST-02-25 (Concluded).

While there is some scatter from the f^{-1} behavior expected, the departures are not great, and the largest departures shown in the two figures are at the end points of the passes and are attributable to detrender effects. Therefore, short of reprocessing a larger number of Stanford passes (note that five passes constitute roughly six percent of the entire Stanford/Wideband data base), we do not feel that there is strong evidence that the residual difference in $\sqrt{C_k L}$ shown in Figure 24 is due to external noise interference on the VHF channel.

Two features in the overall shape of the latitudinal variation of $\sqrt{C_k L}$ for both the Stanford and Bellevue data sets in Figure 24 suggested another possible contribution to the discrepancy: (i) both curves "kink" at latitudes very close to the latitude of the station from which the data were collected, and (ii) the slopes of the high-latitude end of both curves are nearly identical. In examining the data, we found that the kinks occurred at the latitude where the minimum in the longitude-averaged value of the F-layer incidence angle, χ, occurred. Although any variations with χ should be accounted for in the theory that gives T in terms of $C_k L$, we nevertheless replotted the data from Figure 24 as $\sqrt{C_k L} \cos \chi$, as shown in Figure 27. The discrepancy still has not been accounted for, but it has been reduced, and the kink in the Stanford data has disappeared.

One possible explanation for this observed $\sec \chi$-dependence in the $C_k L$ data would be a break-down in the assumption, made in the theory that gives T in terms of $C_k L$, that the irregularity layer is thick with respect to the correlation lengths of the irregularities. This assumption leads to a variation of T with the product of $\sec \chi$ and $C_k L$. If this assumption is not valid, which would imply a coherent integration of the effects of the irregularities on the phase, a $\sec^2 \chi$ variation would result. While this does not agree with the $\sec^3 \chi$ variation suggested in the Stanford $C_k L$ behavior in Figure 27, it is in the correct direction and may imply that the thick-screen assumption is invalid for this data set.

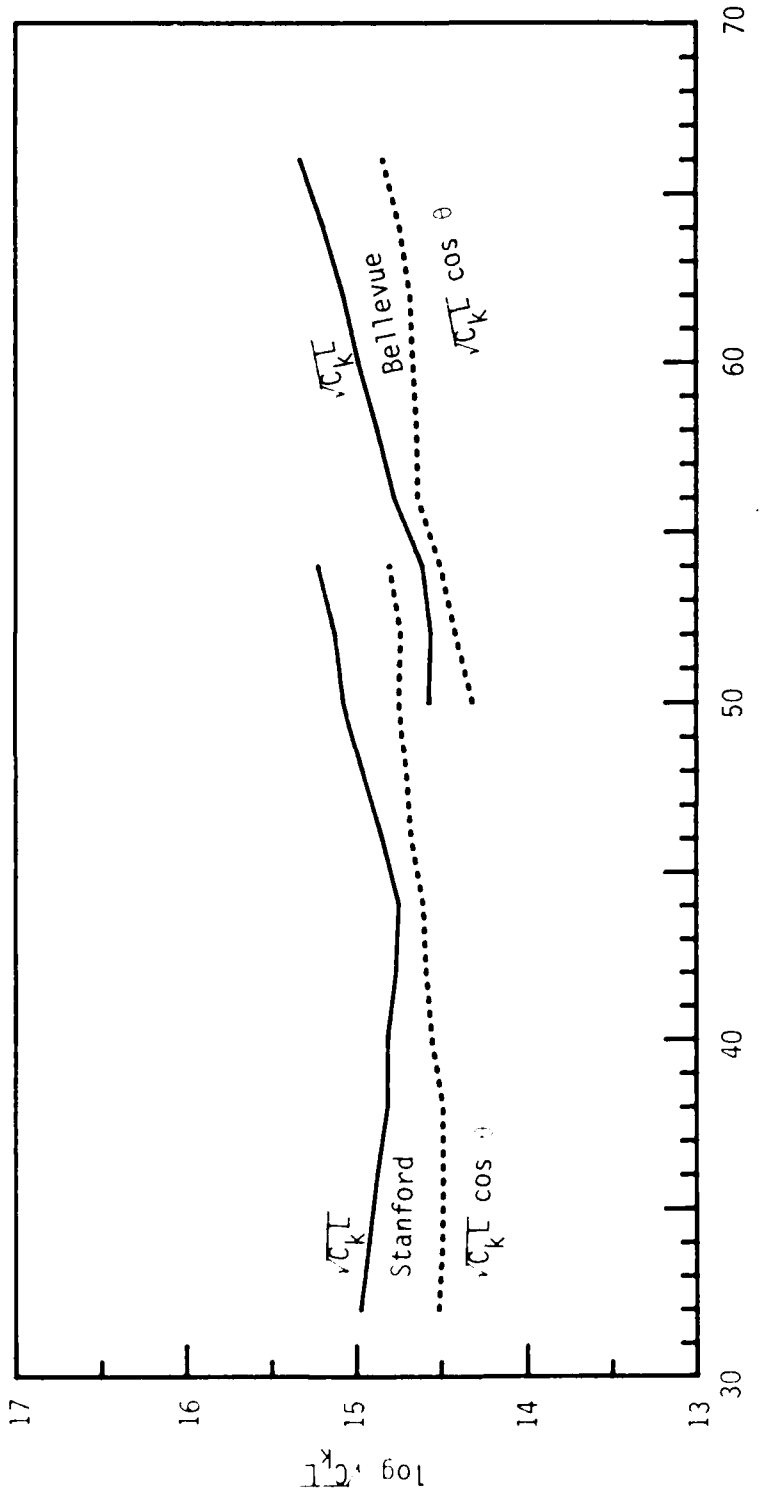

Figure 27. Variation of $\sqrt{C_{kL}}$ and $\sqrt{C_{kL}}\cos\theta$ with apex latitude for the Stanford and Bellevue data bases.

DISTRIBUTION LIST

DEPARTMENT OF DEFENSE

DEFENSE COMMUNICATIONS AGENCY
ATTN A200 R CRAWFORD
ATTN A320 P BIRD
ATTN A730 G JONES

DEFENSE COMMUNICATIONS ENGINEER CENTER
ATTN CODE R123 (TECH LIB)

DEFENSE INTELLIGENCE AGENCY
ATTN DC-7B
ATTN DIR
ATTN DT-1B
ATTN RTS-2B
ATTN VP-TPO

DEFENSE NUCLEAR AGENCY
ATTN NANF
ATTN NAWE
ATTN OPNA
3 CYS ATTN RAAE
ATTN RAAE K SCHWARTZ
ATTN RAAE L SCHROCK
ATTN RAAE T WALSH
ATTN RAEE
4 CYS ATTN TITL

DEFENSE TECHNICAL INFORMATION CENTER
12 CYS ATTN DD

FIELD COMMAND DEFENSE NUCLEAR AGENCY
ATTN FCTT W SUMMA
ATTN FCTXE

JOINT DATA SYSTEM SUPPORT CTR
ATTN C 312 R MASON

STRATEGIC DEFENSE INITIATIVE ORGANIZATION
ATTN KE
ATTN SLKT
ATTN SN
ATTN SY

DEPARTMENT OF THE ARMY

HARRY DIAMOND LABORATORIES
2 CYS ATTN SCHLD-NW-P
ATTN SLCHD-NW-R R WILLIAMS

U S ARMY ATMOSPHERIC SCIENCES LAB
ATTN SLCAS AE E

U S ARMY COMMUNICATIONS R&D COMMAND
ATTN DRDCO-COM-RY W KESSELMAN

U S ARMY FOREIGN SCIENCE & TECH CTR
ATTN: DRXST-SD

U S ARMY NUCLEAR & CHEMICAL AGENCY
ATTN: LIBRARY

U S ARMY SATELLITE COMM AGENCY
ATTN: AMCPM-SC-3

U S ARMY STRATEGIC DEFENSE COMMAND
ATTN: ATC-O W DAVIES
ATTN: ATC-R W DICKSON

DEPARTMENT OF THE NAVY

NAVAL OCEAN SYSTEMS CENTER
ATTN: CODE 532
ATTN: CODE 54 J FERGUSON

NAVAL RESEARCH LABORATORY
ATTN: CODE 4180 J GOODMAN
ATTN: CODE 4700 S OSSAKOW
ATTN: CODE 4720 J DAVIS
ATTN: CODE 4732 B RIPIN
ATTN: CODE 4750 P RODRIGUEZ
ATTN: CODE 4780 J HUBA

NAVAL UNDERWATER SYS CENTER
ATTN CODE 3411, J KATAN

DEPARTMENT OF THE AIR FORCE

AIR FORCE GEOPHYSICS LABORATORY
ATTN LID/J RAMUSSEN
ATTN LIS J BUCHAU
ATTN LS
ATTN LS/R O'NIEL
ATTN LSI/ H GARDINER
ATTN LYD/K CHAMPION

AIR FORCE SPACE TECHNOLOGY CENTER
ATTN XP

AIR FORCE TECHNICAL APPLICATIONS CTR
ATTN TN

AIR FORCE WEAPONS LABORATORY, NTAAB
ATTN NTN
ATTN SUL

AIR FORCE WRIGHT AERONAUTICAL LAB/AAAD
ATTN W HUNT

AIR UNIVERSITY LIBRARY
ATTN AUL LSE

ROME AIR DEVELOPMENT CENTER, AFSC
ATTN OCDS R SCHNEIBLE
ATTN TSLD

DEPARTMENT OF ENERGY

LOS ALAMOS NATIONAL LABORATORY
ATTN D SAPPENFIELD
ATTN D SIMONS
ATTN J WOLCOTT
ATTN MS J ZINN
ATTN R JEFFRIES
ATTN R W WHITAKER
ATTN T KUNKLE

SANDIA NATIONAL LABORATORIES
ATTN A D THORNBROUGH 400
ATTN D DAHLGREN 6440
ATTN ORG 1231 T P WRIGHT
ATTN ORG 314 W D BROWN
ATTN ORG 332 R C BACKSTROM
ATTN SPACE PROJECT DIV
ATTN TECH LIB 3141 (RPTS REC CLRK)

OTHER GOVERNMENT

CENTRAL INTELLIGENCE AGENCY
ATTN OSWR/NED
ATTN OSWR/SSD FOR K FEUERPFETL

DEPARTMENT OF DEFENSE CONTRACTORS

AEROSPACE CORP
ATTN D OLSEN
ATTN E RODRIGUEZ
ATTN I GARFUNKEL
ATTN J KLUCK
ATTN J STRAUS
ATTN K S CHO
ATTN R SLAUGHTER
ATTN T SALMI

AUSTIN RESEARCH ASSOCIATES
ATTN J THOMPSON

BERKELEY RSCH ASSOCIATES, INC
ATTN C PRETTIE
ATTN J WORKMAN
ATTN S BRECHT

EOS TECHNOLOGIES, INC
ATTN B GABBARD
ATTN W LELEVIER

JAYCOR
ATTN J SPERLING

JOHNS HOPKINS UNIVERSITY
ATTN C MENG
ATTN J D PHILLIPS
ATTN J NEWLAND
ATTN K POTOCKI
ATTN R STOKES
ATTN T EVANS

KAMAN TEMPO
ATTN B GAMBILL
ATTN DASIAC
ATTN R RUTHERFORD
ATTN W MCNAMARA

KAMAN TEMPO
ATTN DASIAC

M I T LINCOLN LAB
ATTN D TOWLE L 230
ATTN I KUPIEC L 100

MAXIM TECHNOLOGIES, INC
ATTN J LEHMAN
ATTN J MARSHALL
ATTN J SO
ATTN N CIANOS

MISSION RESEARCH CORP
ATTN B R MILNER
ATTN C LAUER
ATTN C RINO
ATTN D ARCHER
ATTN D KNEPP
ATTN F FAJEN
ATTN F GUIGLIANO
ATTN G MCCARTOR
ATTN K COSNER
ATTN R BIGONI
ATTN R BOGUSCH
ATTN R DANA
ATTN R HENDRICK
ATTN R KILB
ATTN R MORGANSTERN
ATTN S GUTSCHE
ATTN TECH LIBRARY

MITRE CORPORATION
ATTN A KYMMEL
ATTN C CALLAHAN
ATTN D RAMPTON PH D
ATTN M R DRESP
ATTN R DRESP

NORTHWEST RESEARCH ASSOC INC
2 CYS ATTN E FREMOUW
2 CYS ATTN J SECAN
2 CYS ATTN R ROBINS

PACIFIC-SIERRA RESEARCH CORP
ATTN: E FIELD JR
ATTN: F THOMAS
ATTN: H BRODE, CHAIRMAN SAGE

PHOTOMETRICS, INC
ATTN: I L KOFSKY

PHYSICAL RESEARCH INC
ATTN: H FITZ
ATTN: J JORDANO

PHYSICAL RESEARCH, INC
ATTN: R DELIBERIS
ATTN: T STEPHENS

PHYSICAL RESEARCH, INC
ATTN: J DEVORE
ATTN: J THOMPSON
ATTN: W SCHLUETER

R & D ASSOCIATES
ATTN: B LAMB
ATTN: C GREIFINGER
ATTN: F GILMORE
ATTN: G HOYT
ATTN: H ORY
ATTN: M GANTSWEG
ATTN: M GROVER
ATTN: R TURCO
ATTN: W KARZAS

SCIENCE APPLICATIONS INTL CORP
ATTN: C SMITH
ATTN: D HAMLIN
ATTN: E STRAKER
ATTN: L LINSON

SRI INTERNATIONAL
ATTN: D MCDANIEL
ATTN: W CHESNUT
ATTN: W JAYE

TOYON RESEARCH CORP
ATTN: J GARBARINO
ATTN: J ISE

VISIDYNE, INC
ATTN: J CARPENTER

END

8-87

DTIC